NOVEL NON-COHERENT DETECTION METHODS FOR INDOOR RADIO TRACKING SYSTEMS

by

Jiacheng Guo

Submitted in partial fulfilment of the requirements
for the degree of Master of Applied Science

at

Dalhousie University
Halifax, Nova Scotia
January 2018

Dedication

I dedicate this thesis to my beloved parents, Youliang and Fang, and to my girlfriend, Yi.

May their lives be full of love, health, and happiness.

TABLE OF CONTENTS

.

LIST OF TABLES

LIST OF FIGURES

ABSTRACT

Indoor localization systems attract great attention from both academia and industry. However, most existing indoor localization technologies have their own limitations. Either they require user to stay within the line-of-sight of the system (e.g., Kinect) or users have to wear specific wireless devices to get tracked (e.g., radio frequency (RF) systems).

This thesis focuses on development of indoor frequency-modulation-continuous-wave (FMCW) radio tracking system, which can track an indoor user without requiring him/her to wear communicating devices or staying in the line-of-sight of devices.

First, we develop a simulation model of the system. We then obtain a set of tracking results under various channels and find appropriate parameters for securing good tracking performances. Secondly, we propose two novel non-coherent constant-false-alarm-rate (CFAR) detection methods for the system. Parametric studies are conducted on the proposed methods and performances are evaluated under different channels of AWGN, line-of-sight (LOS) and non-line-of-sight (NLOS).

LIST OF ABBREVIATIONS USED

ADC	Analog-to-Digital Converter
AOA	Angle of Arrival
AWGN	Additive White Gaussian Noise
CFAR	Constant False Alarm Rate
DFT	Discrete Fourier Transform
FFT	Fast Fourier Transform
FMCW	Frequency Modulated Continuous Waves
HPF	High-Pass Filter
IR	Infrared Radiation
LOS	Line-of-Sight
LPF	Low-Pass Filter
NLOS	Non-Line-of-Sight
RF	Radio Frequency
RSS	Received Signal Strength
TOA	Time of Arrival

ACKNOWLEDGEMENTS

First, I sincerely thank my supervisor, Prof. Zhizhang (David) Chen, who kindly welcomed me to join his laboratory and provided me with the opportunity to work on this interesting research. I have had a really good time working in the professional environment he has created. It has been my honor to be one of his Master students.

I also want to thank my committee members, Dr. Kamal EI-Sankary and Dr. William J. Phillips, for their reviews of my thesis and their constructive comments and feedback.

I would also like to thank Drs. Zhimeng Xu and Aidong Yang, who have also worked in Dr. Chen's laboratory, for their valuable discussions and suggestions during our projects. I am very grateful for their ideas and instructions.

I want to say thank you to the ECED Administrative Secretary, Nicole Smith, for her friendly help and patience in daily matters.

Finally, I want to thank my parents, Youliang and Fang, and also my girlfriend, Yi, for their consistent support and love.

CHAPTER 1 INTRODUCTION

1.1 Background and Motivation

In recent years, we have witnessed rapid development in localization and tracking systems. As a result, hundreds of new applications are now available, such as Google Maps, Uber, and even the most popular game for 2016, Pokemon Go. Such applications rely on Global Positioning System (GPS) [1], which provides a robust and relatively accurate localization service in an outdoor environment. However, such techniques perform unsatisfactorily when targets are in an indoor circumstance because the buildings significantly block the GPS signal transmissions. Furthermore, compared with the outdoor tracking system, the indoor localization system requires much more accurate and simultaneous location information. For example, an error of a few meters for an APP such as Google Maps may be innocuous; however, for an indoor localization APP, such an error may place a target in a completely different office or building. Hence, motivated by the demands of localization systems that could provide high accuracy and synchronous service in an indoor environment, there is a great surge in studying and developing indoor motion tracking and localization systems. Those systems can be roughly separated in the following three categories: (1) Infrared Radiation (IR) systems; (2) Radio Frequency (RF) location-based systems; (3) Kinect and depth imaging systems.

The most representative and valuable system for IR location-aware system is the Active Badge System [2]. In this system, users wear a badge that transmits a unique IR signal by a constant period. The signal travels through the environment and can be picked up by sensors located in known places inside a building. Based on the IR signals captured by sensors, the system is able to estimate the location of the users [3]. Other similar IR-based localization systems have been proposed for instance, one presented in [4]: the IR transmitters are fixed on ceilings instead of being worn by users while the sensors are carried by users. Although an IR location-aware system has high accuracy in the level of centimeters, it does suffer from several drawbacks. First, the available location range is significantly limited due to the poor transmitting range of the inferred radiation. Secondly, the cost of installation and maintenance is high due to the necessary large numbers of sensors and transmitters. Finally, an IR-based system is strongly affected by sunlight or other indoor lights, which is definitely a tricky problem in a room with windows.

The above drawbacks have led more and more researchers to focus on RF-based localization systems which outperform the IR localization systems in terms of scalability, range, deployment as well as the maintenance. However, such RF systems do have to face another great challenge, multipath propagation. Many methods or techniques are then

developed to deal with this hard-to-predict pattern of multipath propagation. For example, [5]-[8] build maps of the signal strength to eliminate the inferences caused by multipath propagation, while others, e.g., [9] and [10], use RF propagation models to correct errors and improve location accuracy. So far, the averaging accuracy of these RF systems can be achieved around 60 cm [11].

The other prominent indoor tracking technique is called Kinect, published by Microsoft on Nov. 4th, 2010 [51]. Unlike the previous two types of tracking systems, Kinect can track the three-dimensional motion of a human being without requiring them to wear any wireless devices; it uses depth imaging techniques to track the motion of a target. Although this depth imaging technique does free the users from wearing any instrument, it still requires users to stay within the device's line-of-sight. That is if the distance between the devices and users is too wide or if there are obstructions between them, the system will fail to work properly.

Based on the above discussions, we choose to investigate a RF localization system which could achieve the 3D tracking goal without requiring targets to wear any wireless devices. A laboratory at MIT has proposed the RF-based 3D tracking system using frequency-modulated continuous-wave (FMCW) radar signal which can track an indoor object without instrumenting them with any communicating devices. The average accuracy of this system is around 10 to 23 cm [13] – [15]. Such a system has great potential; hence, we focus on it and investigate its performances with different algorithms. We first develop the simulation model with MATLAB and simulate its performances. We then propose two novel non-coherent constant false alarm rate (CFAR) detection methods and evaluated their performance under realistic channel conditions. We compare them with the conventional detection method and reach final conclusions.

1.2 Research Objectives

The primary goal of this thesis is to study and improve the indoor FMCW radio tracking system based on the system proposed by a MIT research group led by Prof. F. Adib [13]. The specific objectives are:

1. Investigate the principle and performance of the indoor FMCW radio tracking system and develop a simulation model using MATLAB software.
2. Simulate and evaluate, with the model developed, performances of the conventional FMCW system under different channel conditions of AWGN, line-of-sight (LOS) and non-line-of-sight (NLOS).
3. Develop novel non-coherent detection methods and incorporate them into the system and evaluate their performances with different parameters under different channel conditions.

4. Compare the performances of the conventional and proposed methods, suggest best system parameters and provide directions of future work for practical implementations.

1.3 Thesis Organization

This dissertation is divided into five chapters. The contents of each chapter are as follows:

Chapter 1 introduces the background, research motivations, and objective goals of this thesis.

Chapter 2 provides a literature review of three existing racking and localization systems: the infrared-based system, the radio-frequency (RF) based system and imaging-based system. Comparisons of them are made in terms of advantages and disadvantages.

Chapter 3 introduces basic operational principle and implementation of the FMCW radar technique in the RF-based location and tracking system. It also presents our development of the MATLAB simulation model for the FMCW location and tracking system, which lays the foundation of quantitate assessments in realistic channel conditions (they have not been done by others in open literature). Simulation results demonstrate the challenges caused by multipath propagation in an indoor environment.

Chapter 4 focuses on detection methods used in the indoor radio tracking system. The first part of the thesis introduces and explains the basic idea of signal detection theory as well as the principle of Constant False Alarm Rate (CFAR) detection. In the second part of this chapter, structure and mathematical model of the conventional detector of FMCW radar system are given and discussed. In the third part, two new non-coherent detection methods based on measurements of Kurtosis and Skewness values are proposed and simulated. Their performances are evaluated and compared under three different channel conditions, additive white Gaussian noise (AWGN), line-of-sight (LOS) as well as non-line-of-sight (NLOS).

Chapter 5 concludes the thesis. Future directions in the proposed research area are also presented in this chapter.

CHAPTER 2 BACKGROUND AND LITERATURE REVIEW

This chapter provides background about the tracking and localization systems. Based on the information, we illustrate two typical indoor localization systems, one of which is the in-building RF-based user location and tracking system and the other is the depth imaging system (Microsoft Kinect sensor).

2.1 Three Typical Localization Methods (or Algorithms)

As mentioned before, there are three types of indoor tracking and localization systems, IR-based systems, RF-based systems, and the depth imaging systems. The tracking and location algorithms they used can also be categorized into three different types: the received signal strength (RSS) based method, the time-of-arrival (TOA) based method, and the angle-of-arrival (AOA) method.

In a RSS method, a system relies on the strength of received signals to locate a target. Because the power of wireless radio will decay with the signal transmission distance following a specific attenuating equation, we can use the RSS to deduce the travel distance of the radio signal based on the equation and hence estimate the position of the object. However, RSS algorithm will be greatly affected by multipath propagation interferences in an indoor environment because multiple copies of the transmitted signal are received at a receiver through unpredictable multipaths and the power of the received signal will differ dramatically from what is expected for a single path signal. In this situation, the estimated results may contain non-negligible errors [16] even with the correcting algorithms for multipath effects [8].

In a TOA-based method (it is also called Time of Flight (TOF) [13]), the total signal transmitting duration of the signal is estimated. Since we know the traveling speed of the signal, the distance between the object and a transmitting device can be calculated. The TOA method is very popular for underwater sonar localization systems [17]. However, when it comes to the indoor radio tracking and location system, the situation becomes quite tricky. Not only are there multipath signal interference in an indoor environment, but also the speed of radio signal is extremely high, which makes TOA extremely short and hard to detect directly. To address the difficulty, methods such as FMCW have been proposed where TOA is detected or measured indirectly.

As for the AOA-based system, it uses the Angle of Arrival (AOA) to estimate the location of a target. More specifically, it employs an array of smart antennas and uses the signals received at each array antenna element to pinpoint the location of a target [18]. However, such AOA-based localization systems are not very popular for the indoor tracking system due to the following three reasons. First, the smart antenna arrays that could estimate the AOA are usually very expensive and hence are not practical for the large scale indoor localization system. Secondly, size of a smart antenna array is relatively too large for an indoor application. Thirdly, multipath effects still have distinctly negative effects on the performance of the AOA-based localization systems.

Based on the above analyses, in the following subsections, we present the reviews of an RF based indoor tracking and location system that uses the RSS techniques and the Microsoft Kinect sensor system. Both of them are considered widely for possible practical applications.

2.2 The RF-Based User Location and Tracking System

The RF-based indoor user localization and tracking system under consideration was first proposed by P. Bahl and V. Padmanabhan in 2000 [8]. It uses RSS-based localization method and its operational principle has been applied since it was first proposed.

In [8], the entire experiment testbed is the second floor of a 3-storey building, where three base stations are set up in specific known locations. A mobile host carried by a user walking around the second floor keeps transmitting the wireless signal which are expected to be received by the three base stations. The signal strength (SS) information of this wireless signal is recorded as a function of the user's location. After the experiment, the authors collect the SS data at 70 distinct physical locations in four different directions. Along with this SS data, the layout of the second floor is recorded and a simulation model is set up which could estimate how many walls stand between the base stations and a location. Such information is for building an accurate radio location algorithm.

There are two main RSS-based algorithms developed for the RF-based localization system, the empirical method and radio propagation model.

The empirical method is quite straightforward. Since enough SS information samples covering the second floor have been collected, they are used as references for the received SS data. The sample that best matches the observed SS data presents the estimated location of a target. The method is easy to implement and has relatively accurate performance around 2.9m. However, it has two drawbacks. First, it requires significant efforts to set up the SS measurements for every physical environment. Secondly, such efforts may need to be repeated when the circumstance changes, e.g., the relocation of a base station.

Due to those limitations of the empirical method, an alternative method was proposed to overcome those drawbacks, the radio propagation modeling. The main idea of it is to generate a set of theoretically-computed SS data which replace the experimental database. The method then estimates the position of the object by matching the SS information observed in real-time to the theoretically-computed SS data. It is apparent that the performance of this method is directly determined by how well the radio propagation model simulate the practical situation. The results show that the radio propagation model can provide up to a resolution of around 4.3m, compared with a resolution of 2.9m for the empirical method.

In summary, two RSS-based localization algorithms have been proposed so far. Although the empirical method outperforms the radio propagation model in terms of accuracy, the latter make deployment and maintenance much easier and cheaper.

2.3 Microsoft Kinect Sensor

On Nov. 4th, 2010, Microsoft launched its novel gaming device, Kinect, for Xbox 360 Play Station. The original purpose of Kinect sensor is to revolutionize the entertainment experience of the players with Kinect; players can interact with the games directly, using their bodies. Such function is achieved by the depth imaging camera of the Kinect sensor which makes it possible for the computer to directly sense the third dimension (depth) of players and the environment. In this way, the computer can understand what a player is doing and then makes correct response to those behaviors. Although the primary application of Kinect is focused on the gaming industry, the impact brought by Kinect has extended far beyond its initial interests. For the electrical engineering realm, the most exciting and meaningful impact generated by Kinect is the way that the Kinect sensor detects and tracks the location and motion of the target. Here we briefly introduce and describe the principle of the Kinect sensor.

The structure of the Kinect sensor is shown in Figure 2-1. It contains several advanced sensing devices, including an IR projector, a RGB camera, and an IR camera. The depth sensor is made up of the IR projector and the IR camera. First, the IR projector projects the IR signal through a diffraction grating which turns into a set of IR dots. Because the relative geometry between the IR projector and the IR camera as well as the IR dot pattern are known, an image in 3D can be reconstructed by matching a dot observed in a picture with a dot in a projector pattern [12]. In this way, the Kinect sensor is able to draw a depth map.

Figure 2-2 presents a depth image captured by the Kinect sensor, in which the darker a pixel is the closer the distance between the point and the camera will be. The pure black pixel indicates that there is no information about the depth value at that space. From Figure 2-2, it is clear that there are two persons in this image. In the top right corner, there is no

reflector in that space. By using the depth value generated by the depth sensor, real depth can be calculated between the spots in the image and the devices, and hence track the motion of a user.

Figure 2-1. The structure of Microsoft Kinect sensor [12]

Figure 2-2. Depth image of the Kinect sensor [12]

As for tracking algorithm, instead of trying to track the human as an entire object, the Kinect uses different joints to represent the human body: each of the joints refers to a different part of human body, such as the head, neck, shoulder, hands, and then tracks each

joint independently. This algorithm, called skeleton tracking, greatly decreases the amount of calculation and is computationally efficient.

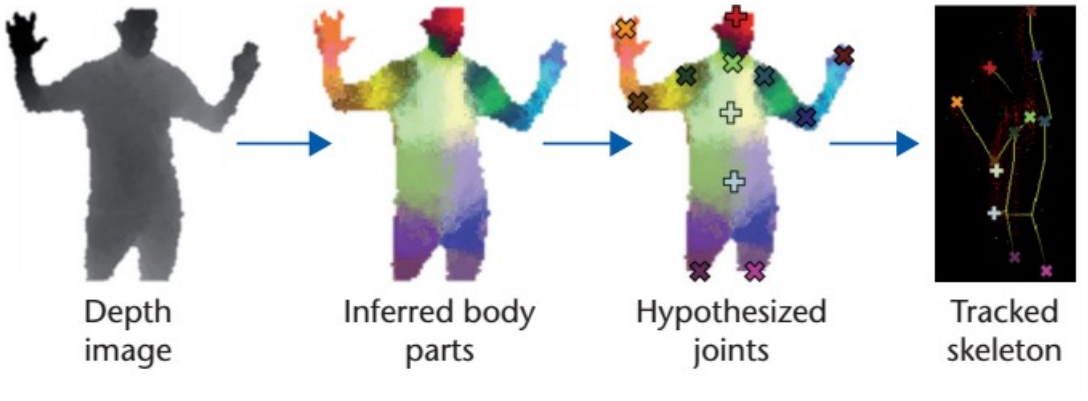

Figure 2-3. The process of Kinect skeleton tracking [12]

Figure 2-3 illustrates the process of the process clearly. First, he depth image by the depth senor is obtained. Then, the human body is separated into several representative parts. After that, center of every representative part as the body joints is determined with a mean shift algorithm. Finally, all of the joints are combined into one integral skeleton map and the motion is tracked entirely [12].

Kinect has great impacts on the modern indoor localization technology. It provides us with a novel way to track the motion of a target with low complexity and wide availability. With it, many new applications have been proposed in computer science and electrical engineering, especially for robotics industry.

2.4 Conclusion

Chapter 2 briefly reviews three typical types of localization and tracking systems, RSS, TOA and AOA methods. It then describes two RSS-based location algorithms and Microsoft Kinect system for tracking and location. Their advantages and disadvantages are indicated, respectively.

CHAPTER 3 THE INDOOR FMCW RADIO TRACKING SYSTEM

In this chapter, we will focus on the radio tracking system that uses frequency-modulated continuous-wave (FMCW) to locate a target (typically, a person). The organization of this chapter is as follows: first, we show how to use the FMCW radar signal to estimate the propagation delay; then we introduce the problems caused by multipath propagation and propose possible solutions; we simulate and examine the FMCW location and tracking in two dimensions.

3.1 Measurement of the Propagation Delay

An indoor radio tracking system uses radar signal to measure the propagation time delay τ between the transmitted signals and received echoes. The measured τ, also called as the time of flight (TOF) or time of arrival (TOA) [19], is then applied to calculate the propagation distance of the FMCW signal and therefore the location of a target.

The direct way to calculate the propagation delay is to emit a very short impulse and then estimate the time of flight between this transmitted impulse and its received echo in time domain [13]. Since the tracking systems under consideration work in the indoor environment, distance between a target and the RF transmitter/receiver is normally within 50m. As a result, the propagation delay is extremely small since the propagation speed of a radio wave is the speed of light. To detect such a small delay, the system requires high speed analog-to-digital converters (ADC), usually operating at GHz. Because GHz ADCs are power-consuming and expensive, direct measurement of the delay is not practical. Therefore, FMCW radar technique is developed to estimate the propagation delay in a indirect manner. The following two sections, 3.1.1 and 3.1.2, describe the theory and implementation of FMCW radar system respectively.

3.1.1 Theory of FMCW Radar System

For FMCW, the transmitted waveform has a constant amplitude, but a linear sawtooth variation of frequency with time. Such linear variation of frequency with time is often referred to as a chirp [20]. According to [21], the term ‘chirp’ was first used by B. M. Oiliver in an internal Bell Laboratories Memorandum entitled ‘Not with a bang, but a chirp’. It is shown in Figure 3-1.

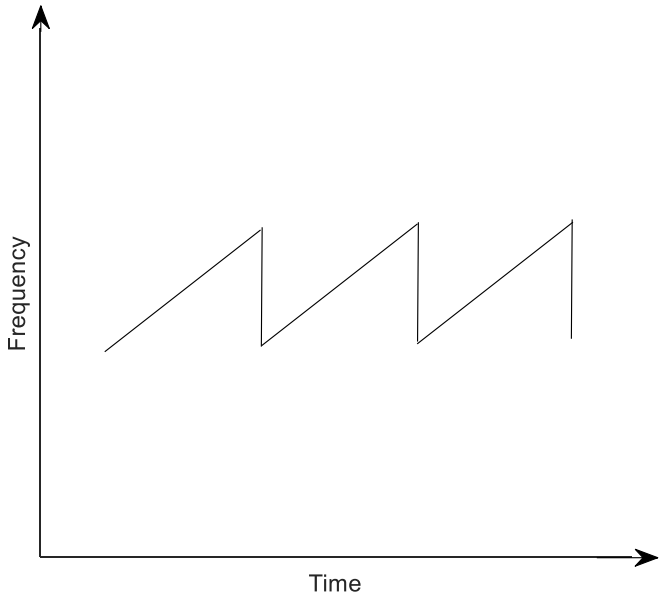

Figure 3-1: FMCW radar signal (chirp signal)

From the linear frequency variation with time, the propagation delay can be computed by comparing the frequency difference between the emitted signal and its received echo. This frequency shift or difference between a transmitted signal and its echo is also called beat frequency [19]. In other words, in a FMCW radar system, measurement of the delay in time domain is transferred into measurement of the frequency different in frequency domain. Such transformation is worthwhile and beneficial because instead of trying to measure the delay in time directly, which requires high speed ADC, the beat frequency (f_{beat}) between the transmitted signal and received signal, whose range is usually MHz, is measured. Therefore, the ADC used becomes much less demanded with lower power consumption and cost since it only needs to operate at multi-MHz.

Suppose that the frequency of the emitted FMCW radar signal varies linearly from f_c to $f_c + B$ in one period of time T_m, as shown in Figure 3-2. Assume that f_{beat} is a frequency difference (or beat frequency) between the transmitted signal T_x and the received echo signal R_x (that is bounced off a target). Then, the propagation delay between the received echo signal and transmitted signal can be calculated as [20]:

$$\tau = \frac{f_{beat} \cdot T_m}{B} \quad . \tag{3-1}$$

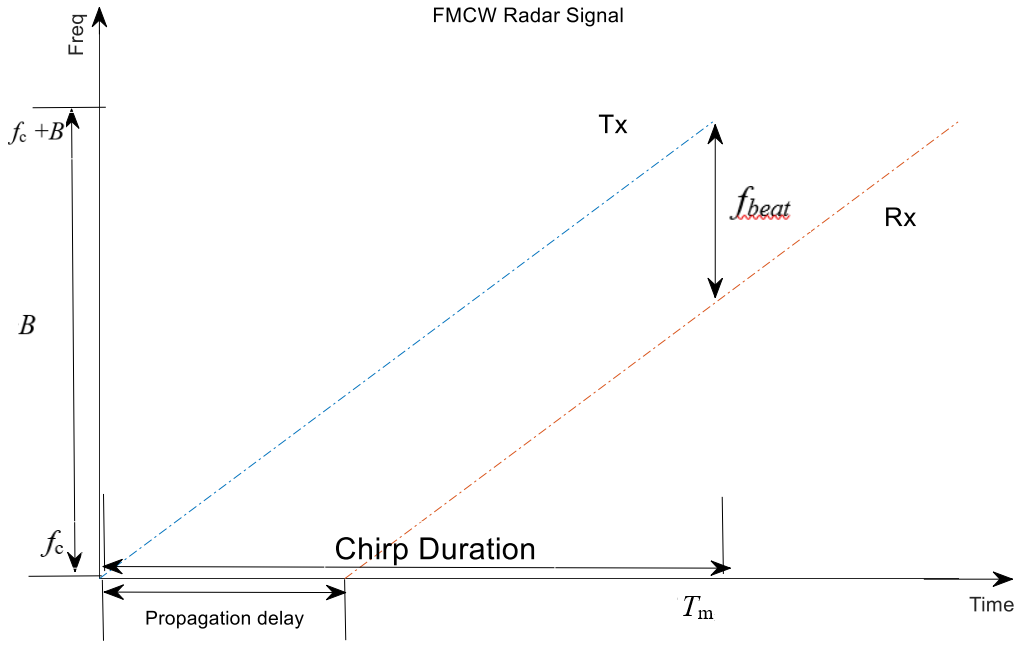

Figure 3-2: Principle of the FMCW radar signal (chirp signal)

Equation (3-1) is based on a single reflection from a target. There are multipaths for a transmitted signal to propagate back to the receiver. In other words, there may be many echoes captured in an indoor environment due to reflections from multiple walls; each of the echoes has its own beat frequency due to different delays in time through different paths [13]. Hence, all of these beat frequencies can be extracted by taking a Fourier Transform of the signal received that contains many echoes of different beat frequencies. This is normally referred as multipath effect. If the multipath effect is not properly handled, incorrect results may be obtained. The issues of multipath effects are described in Section 3.3. In the next subsection, we will discuss the generation of the FMCW.

3.1.2 Signal Generator of FMCW

The structure of the signal generator is presented in Figure 3-3: the FMCW signal whose carrier frequency varies linearly over a wide bandwidth with time has been obtained by a voltage-controlled oscillator (VCO). Since the frequency of the output signal of the VCO is proportional to its input voltage, we obtain our desired FMCW signal by changing the value of the input voltage of the VCO linearly. However, this method has an obvious drawback in that even a very small variation in the input voltage may cause a significant non-linearity in the output frequency [13]. Thus, according to [13], a feedback mechanism has been designed to solve this problem. First, a digital synthesizer is used to generate a highly accurate reference signal. Then the output signal of the VCO is compared with this

reference signal and the offset between these two signals is used to adjust and control the VCO. Although the frequency of output signal sweeps over a relatively wide bandwidth, e.g., from 5.46 to 7.25 GHz [14], the reference signal does not need to sweep over the same relatively wide spectrum because a frequency divider is employed to process the output signal of the VCO before we compare these two signals. The relation between the frequency of input signal and output signal of the frequency divider is [22]:

$$f_{out} = \frac{f_{in}}{n} \quad , \tag{3-2}$$

where n is the integer parameter, f_{in} is the frequency of the input signal, and f_{out} is the frequency of the output signal. Thus, if n is set to be 40, the reference signal only needs to change in a relatively narrow bandwidth from 136.5 to 181.25 MHz, which is much more realizable and power-saving in practice.

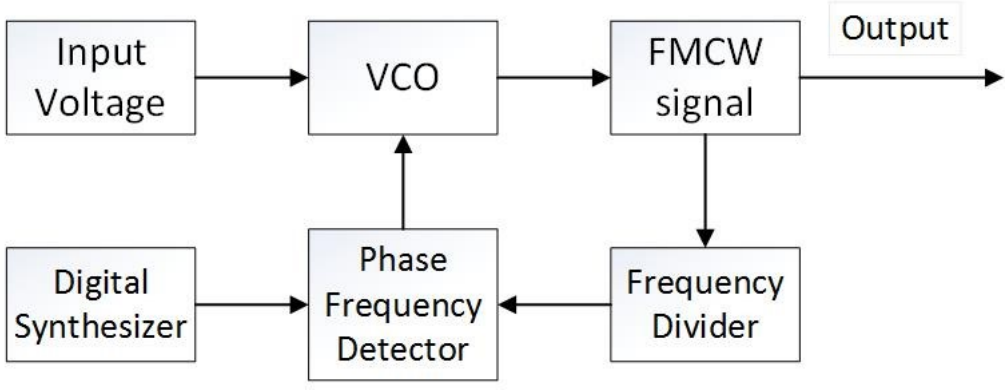

Figure 3-3. The structure of FMCW signal generator

The reason why we choose such particular bandwidth (5.46 to 7.25 GHz) is that this is the widest contiguous spectrum below 10 GHz, which is available for academic study according to the Federal Communication Commission (1993) [23]. The maximum bandwidth of the FMCW radar signal plays a crucial role in the localization resolution. The details and reasons why we have to set the sweeping bandwidth as wide as possible will be discussed in next subsection.

3.1.3 Resolution of FMCW Radar System

According to [24], the FMCW radar system resolution depends mainly on the entire bandwidth that the carrier frequency of the FMCW signal sweeps. This can be proved as follows. First, based on [24], the definition of the resolution is the ability to identify two

nearby locations, in other words, the ability to distinguish the minimum propagation delay between these two independent locations. Therefore, the resolution can be expressed as:

$$Resolution = c\frac{\tau_{\min}}{2} \quad , \tag{3-3}$$

where c is the speed of light, $\tau_{\min}$ is the minimum propagation delay that the system can detect. The factor 2 is caused by the fact that a signal has to travel the path back and forth from antennas to a target. Since the propagation delay is proportional to the beat frequency between the transmitted signals and received echoes, the minimum propagation delay is decided by the frequency resolution a FMCW can resolve. Importantly, in our simulation, we use FFT not DFT to obtain the beat frequency. Otherwise, the FFT bin cannot be calculated as follow. If the FFT is taken, it is the FFT resolution that needs to be considered. According to [25], when we take N_{FFT} points FFT calculation over a single chirp duration T_m, the FFT bin can be calculated as:

$$FFT_{bin} = \frac{F_s}{N_{\text{FFT}}} = \frac{F_s}{F_s \cdot T_m} = \frac{1}{T_m} \quad , \tag{3-4}$$

where F_s is the sampling rate of the ADC.

By combing Equation (3-3) and (3-4), the resolution of a FMCW radar system becomes:

$$Resolution = c\frac{\tau_{\min}}{2} = c\frac{FFT_{bins}}{2 \cdot slope} \quad , \tag{3-5}$$

where the slope is equal to [21] (see also Fig. 1):

$$slope = \frac{B}{T_m} \quad . \tag{3-6}$$

By substituting (3-6) into (3-5),

$$resolution = \frac{c}{2B} \quad . \tag{3-7}$$

where B is the maximum frequency shift of the FMCW radar signal (as shown in Fig. 1).

From Equation (3-7), we can easily come to the conclusion that the resolution of the FMCW radar system is the function of the maximum bandwidth that the carrier frequency sweeps. Since the speed of light is extreme fast, in order to get a high resolution of the tracking system, e.g., at centimeters, it requires the chirp signal to sweep over a very wide spectrum, for example, at multiple GHz. This explains why we choose the FMCW system that sweeps a maximum bandwidth of 1.69 GHz from 5.56 GHz to 7.25 GHz in implementation, simply because this is the largest bandwidth below 10 GHz for the public to implement and study [14]. As a result, the resolution of our system is 8.8 cm calculated by Equation (3-7).

3.2 The Implementation and Analysis of Indoor Radio Tracking System Using FMCW Radar Signal

3.2.1 Implementation

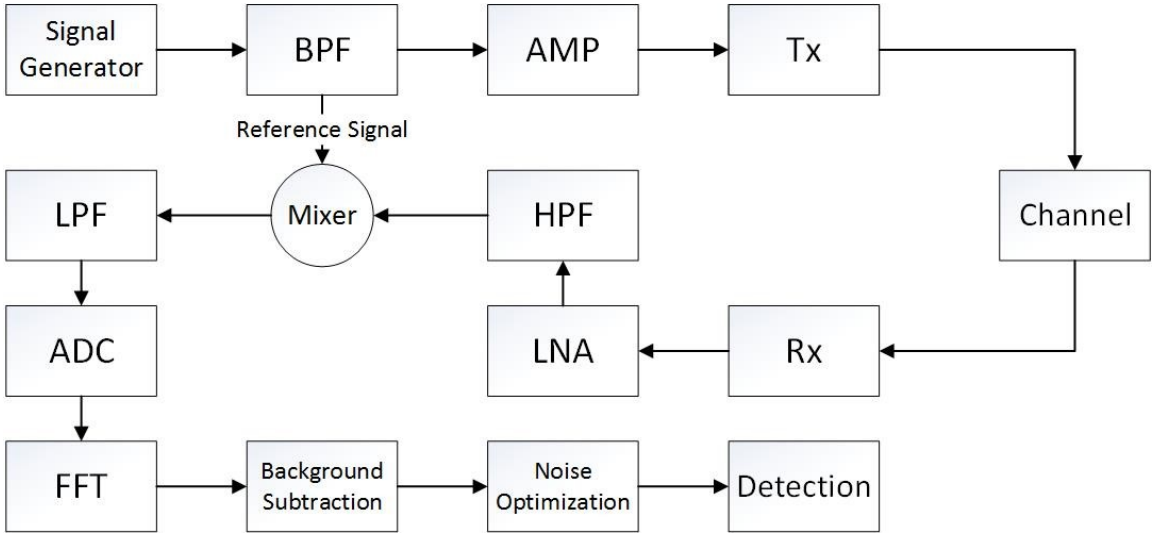

Figure 3-4. The implementation of the Indoor FMCW Radio Tracking System

The implementation of this Indoor Radio Tracking System is shown in the schematic of Figrue 3-4 [19]. First, an FMCW signal is generated, whose frequency linearly sweeps from f_c to f_c+B in the duration T_m (shown in Figure 3-2). Then the signal goes through the band-pass filter (BPF) and is separated into two parts. A small portion goes into a mixer where it is used as a reference signal for detection of the echo signal. The other larger

portion of the generated signal passes through the amplifier and is then emitted by transmitting antenna with gain of G_T.

At the receiver, the signal is captured by the receiving antenna and then goes through the low-noise amplifier with gain G_R and a high-pass filter to increase the signal-to- noise (SNR). Then this received signal is mixed with the reference signal and filtered by a well-designed low-pass filter (LPF); the purpose of the filter is to eliminate the high frequency portion so the remaining signal only contains the signal of f_{beat}. The signal can then be sampled at a low frequency (multi-MHz).

The Fast Fourier Transform is applied to the low-pass filtered signal in order to find the beat frequency between the transmitted signal and received signals. As mentioned before, there will be not only one direct reflected signal (or one echo) bounced off by the target but many other echoes caused by multipaths or reflections by different objects. To eliminate the multipath effects and identify the correct reflected signal caused by the target from these unknown and unpredicted echoes, we can use a background subtraction module [13]. The theory and principle will be discussed in section 3.3. After we eliminate the influence of multipath effect, a detection technique can be used to find the position of the beat frequency in the frequency domain, calculate the propagation delay using Equation (3-1) and then estimate the location of a target.

3.2.2 Mathematical Analysis

In this subsection, we will present the mathematical analysis of the FMCW system.

From Figure 3-2, we see that the frequency increases linearly with the time; the instantaneous frequency of the signal can be written as:

$$f(t) = f_c + \frac{B}{T_m} t \quad . \tag{3-8}$$

The phase of the transmitted FMCW signal is then

$$\phi(t) = 2\pi f_c t + \pi \frac{B}{T_m} t^2 \quad . \tag{3-9}$$

Therefore, the transmitted signal $x(t)$ is [26]:

$$x(t) = \sqrt{2p_t}\cos\{\phi(t)\} = \sqrt{2p_t}\cos(2\pi f_c t + \pi\frac{B}{T_m}t^2) \quad , \tag{3-10}$$

where p_t is the power of the transmitted signal $x(t)$, f_c is the carrier frequency, B is the maximum sweep frequency and T_m is the sweep duration.

After the signal has been emitted by the transmitting antenna, it goes through the multipath channel and is bounced off by the target and then captured by a receiving antenna with gain of G_r. The received signal can be expressed as [26]:

$$r(t) = \sqrt{2p_r}\cos\{\phi(t-\tau)\} = \sqrt{2p_r}\cos\{2\pi f_c(t-\tau) + \pi\frac{B}{T_m}(t-\tau)^2\} + n(t) \quad , \tag{3-11}$$

where p_r is the power of receiving signal, τ is the propagation delay (or TOA) and $n(t)$ represents noises. Here we do not consider multipath effects yet. Multipath effects will be discussed in Section 3.3.

As explained before, the received signal $r(t)$ is mixed with a portion of the transmitted signal $x(t)$. We then have the mixed signal:

$$\begin{aligned} m(t) &= x(t)\cdot r(t) = \sqrt{2p_m}\{\cos[\phi(t)+\phi(t-\tau)] + \cos[\phi(t)-\phi(t-\tau)]\} + n(t) \\ &= \sqrt{2p_m}\cos(2\pi\frac{B\tau}{T_m}t + 2\pi f_c\tau - \pi\frac{B}{T_m}\tau^2) + high\ frequency\ terms) + n(t) \end{aligned} \quad . \tag{3-12}$$

Let the above signal go through a well-designed low-pass filter whose band width is:

$$BW_{low-pass} = \frac{B}{T_m}\tau_{\max} = \frac{B}{T_m}\frac{2d_{\max}}{c} \quad , \tag{3-13}$$

where d_{max} is the maximum target range the FMCW system is designed to detect and $\tau_{\max} = \frac{2d_{\max}}{c}$ is then the corresponding maximum propagation delay the FMCW system can detect. Equation (3-13) is then the maximum frequency shift of the reflected signal from the target.

After the low-pass filter, the signal becomes [19]:

$$y(t) = \sqrt{2p_y}\cos(2\pi f_{beat}t + 2\pi f_c\tau - \pi\frac{B}{T_m}\tau^2) + n_y(t) \quad . \tag{3-14}$$

p_y is the power of the signal power after the low-pass filter. $f_{beat} = \frac{B\tau}{T_m}$. n_y is the noise.

Once the beat frequency f_{beat} is found, the range of the target can be found as

$$d = \frac{cT_m}{2}\frac{f_{beat}}{B} \quad . \tag{3-15}$$

In other words, we first find the beat frequency $f_{beat.}$. We then find propagation delay τ and finally range d of a target. This is how this FMCW radio tracking and location system works.

In the above analysis, we do not consider the multipath effect that exist in an indoor environment. In the flowing subsection, we will discuss the multipath effect.

3.3 Multipath Effect

The discussion and derivation in section 3.2.2 is only for the signal directly reflected from the target. In reality, many echoes reflected from many objects in an indoor environment through different propagation paths; they are all captured by the receiving antenna of an FMCW system at the same time. Thus, the received signal at a specific time is a linear combination of multiple reflections. Each of them is shifted by a certain f_{beat} that is relative to its own TOF though a propagation path. The challenge is to separate the signal reflected directly by our target from all these reflected signals and use its corresponding beat frequency to locate the target.

3.3.1 Types of the Multipath Components

To eliminate this 'Multipath Effect', we can first analyze sources of these echoes due to multipaths. There are actually two kinds of echoes or reflections captured by the receiving antenna, the static reflections and the dynamic reflections [13]. Just as the name indicates, the static reflections refer to the received echoes which are only bounced off static objects in the environment such as furniture or walls. They do not contain any information about

the target that we want to locate. For the dynamic reflections, it represents all of the reflected signals caused by the desired target which may be moving. Such signals include both the signal directly from the target as well as the signals caused by the target but traverse through other different paths and finally arrive at the receiving antenna.

Note that it is worth to point out that in this paper, only one moving target is considered. For multi-target tracking, the situation becomes more complex and is one of the future research directions.

3.3.2 Methods to Resolve the Multipath Issue

As discussed above, there are two kinds of reflections existing in an indoor environment, the static reflections and dynamic reflections. We now describe the methods to resolve them.

For the reflections caused by static objects, the key to solve such problems relies on the characteristic of static objects. Recall form the previous section, for every reflected signal captured by the receiving antenna, it has its own frequency shift which is linearly proportional to its propagation delay. Because the static reflectors do not move over time, it means that the position of its beat frequency do not change in the FFT results with time. Therefore, we could eliminate them by simply taking a measurement when the target of interest is removed from an indoor environment and the measurement with the target in the environment. We then subtract the FFT frame when the target is in the environment from the FFT frame when there is no target in the environment. Such an algorithm is called background subtraction which remove the effects of static multipath reflections.

After eliminating the static reflections, we have to deal with the echoes or reflections bounced off the target, since there is not only one directly reflected signal but many of others indirectly reflected from the moving target, arriving at the same receiving antenna through different multipaths. To differentiate them, the most direct and obvious way is to use signal power to identify the directly reflected signal from other multipath reflected signals [29], because the directly reflected signal has normally the shortest path and thus tends to have the strongest power. This is, however, not always true since there are many objects and it becomes quite possible that a reflected echo that goes through an indirect path may have stronger power than the direct reflected signal which may be significantly attenuated after traversing a wall as an example.

As a result, the author of [13] came up with another method to deal with the dynamic reflections. It is based on the fact that among echoes or reflected signals captured by the receiving antenna at a specific time, the directly reflected signal is expected to travel through the shortest path between the transmitting antenna and receiving antenna.

Therefore, the directly reflected signal will have the smallest frequency shift in the frequency domain with the FFT calculations. In other words, to find the direct reflected signal is to find the peak with the smallest frequency shift in the FFT spectrum and apply this frequency shift to estimate the propagation delay and the range of the target.

3.3.3 MATLAB Simulation

Based on the above discussions, we set up the MATLAB simulations as described below. The parameters we used in the MATLAB simulation is in the following table:

Table 3-1 Simulation Parameters

Parameter	Value	Parameter	Value
f_c (GHz)	5.56	F_s (GHz)	20.0
T_m (ms)	2.5	E_p/N_0(dB)	15.0
B (GHz)	1.69	$BW_{low\text{-}pass}$(kHz)	300
d (m)	20.0	N_{FFT}	$2.5\text{x}10^5$
$d_{\max}$ (m)	50.0	$BW_{high\text{-}pass}$(GHz)	5.0

In the above table, d is the distance between the target and the transmitting and receiving antennas that are collocated at the same position. $d_{\max}$ is the maximum range the tracking system is designed to detect. E_p/N_0 is the signal to noise for equation (3-14), $BW_{low\text{-}pass}$ is the passband of the low-pass filter. N_{FFT} is number of the FFT points computed, and $BW_{high\text{-}pass}$ is the passband of the high-pass filter.

As can be seen, although the sampling rate F_s is as fast as 20 GHz, the real sampling rate of ADC can be relatively low in practice, usually at multi-MHz. As discussed before, this is because the received signal goes through the low-pass filter, the relatively low beat frequency needs to be extracted.

Figure 3-5 shows the flow chart of MATLAB simulation of the Multipath Effect elimination. First, we generate a well-designed chirp signal, of which, frequency shifts from f_c to f_c+B in the duration of Tm. Then we split it into two parts, the small portion used as a reference signal, and the large portion will be emitted by the transmitting antenna.

As for the channel model in simulation, we use 802.15.4a standard published by IEEE [30]. The 802.15.4a standard provides models for the following frequency ranges and environments: for the frequency range from 2 to 10 GHz, it has different models for indoor

residential, indoor office, industrial, outdoor, and open outdoor environments (usually with a distinction between LOS and NLOS properties). We employ CM3 model which is an indoor office environment with LOS condition. To be specific, in the simulation, we first generate several static reflectors, whose range to the antennas is a random number but smaller than d_{max}. Then, for each static reflector and the target reflector, we use CM3 model to generate their own multipath reflected signals, insert and add them to the channel signals to be received by the receiving antenna (see Fig. 3-5).

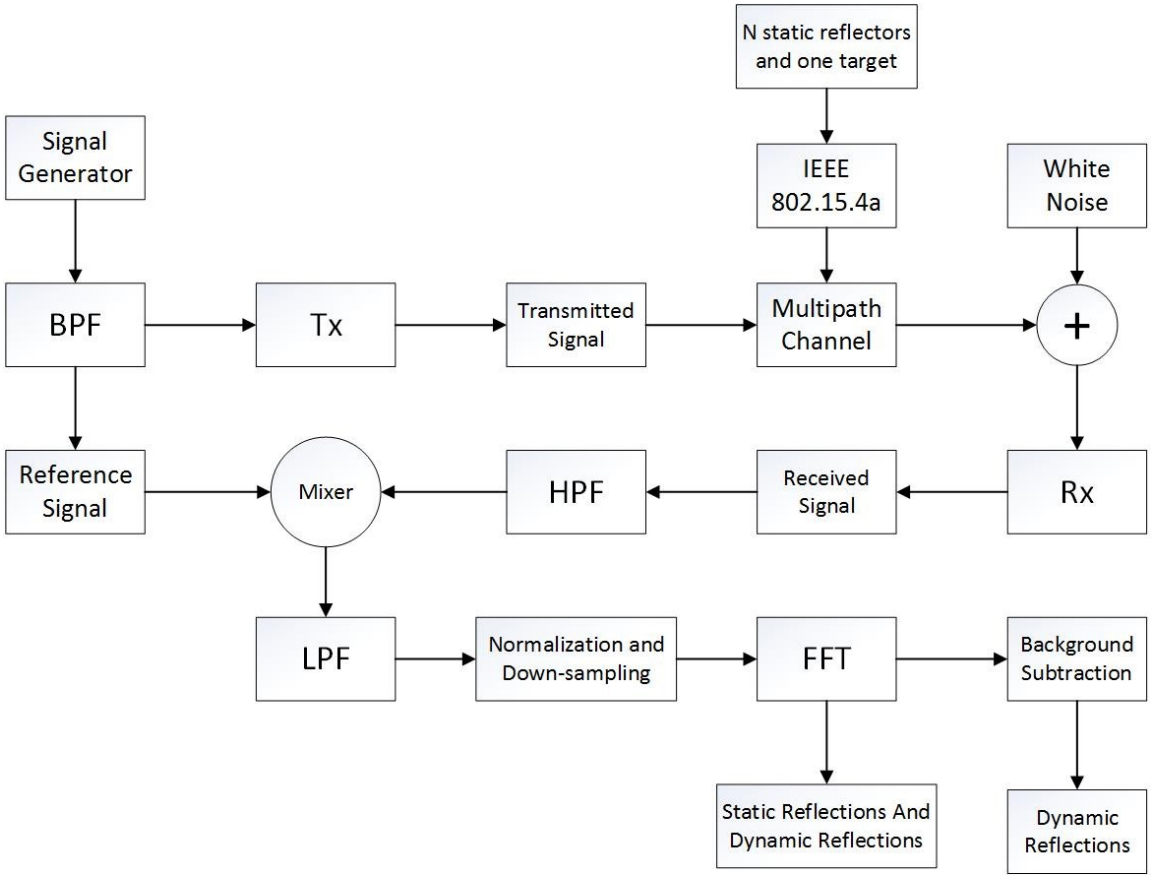

Figure 3-5. The flow chart of MATLAB simulation of the multipath effect

After the signal goes through the channel with the multipath signals, white Gaussian noise is added; the combined signal, representing the practically received signals with noises and multipath signals, is sent to the receiving antenna. The detection processing then follows.

Fig. 3-6 to Fig. 3-8 are the simulation results. Figure 3-6 shows the FFT results of the static reflections (when there is no target in the environment). From the figure, we see that there are many peaks in the FFT frequency domain. Each of them represents a different reflected signal bounced off by different static objects through different paths.

Figure 3-7 shows the FFT results of all the reflected signals captured by the antenna (including both static reflections and dynamic reflections). Comparing this figure with Fig. 3-6, we can see that there are new peaks shown, marked by the red rectangular window. These peaks represent all the reflected signals caused by the target which arrive at the antenna through different paths – multipath effects.

Figure 3-8 shows the results after we subtract all the static reflections of the FFT results of Figure 3-6 with normalized power. We could see that after the subtraction algorithm, there are only some reflected signals caused by the target. Thus, we could use different detection methods to find the target peak in Figure 3-8. For example, the most simple and direct way to find the target peak is to set a threshold, as shown in Figure 3-8. The first peak that is larger than this threshold corresponds to the directly reflected signal caused by the target, and hence, we can use its corresponding frequency to estimate the TOF. The details of different detection methods will be discussed in Chapter 4.

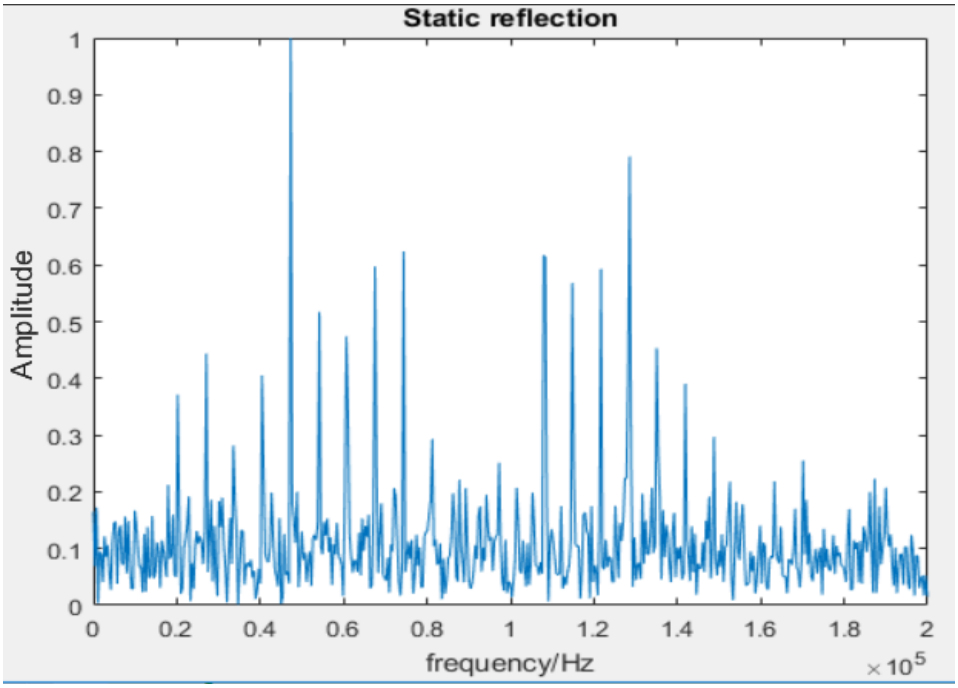

Figure 3-6. FFT results of static reflections (no target)

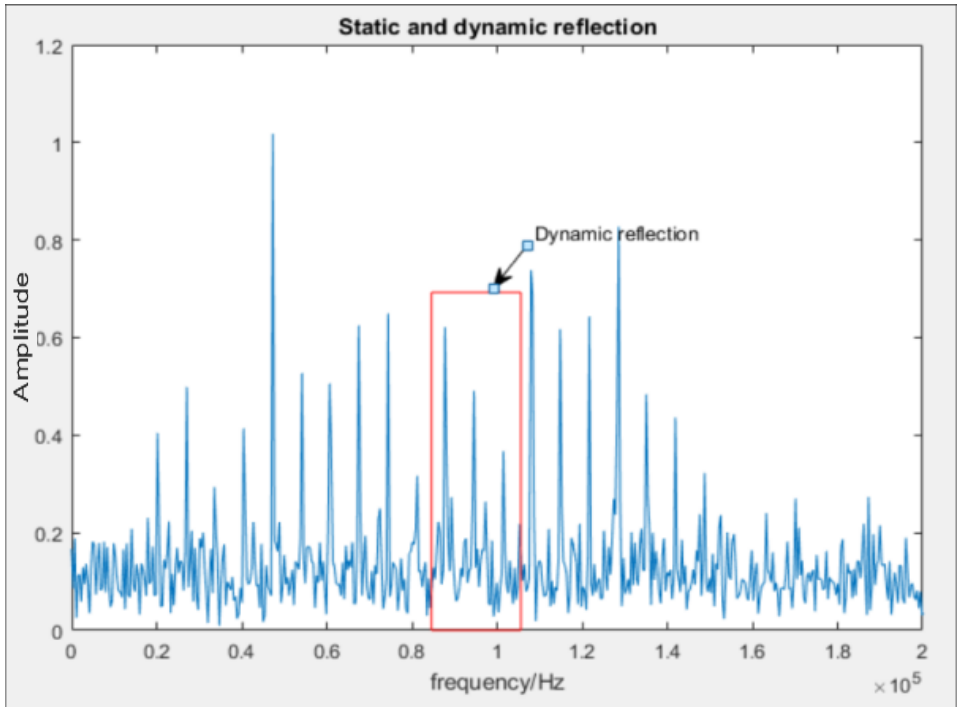

Figure 3-7. FFT results of static and dynamic reflections

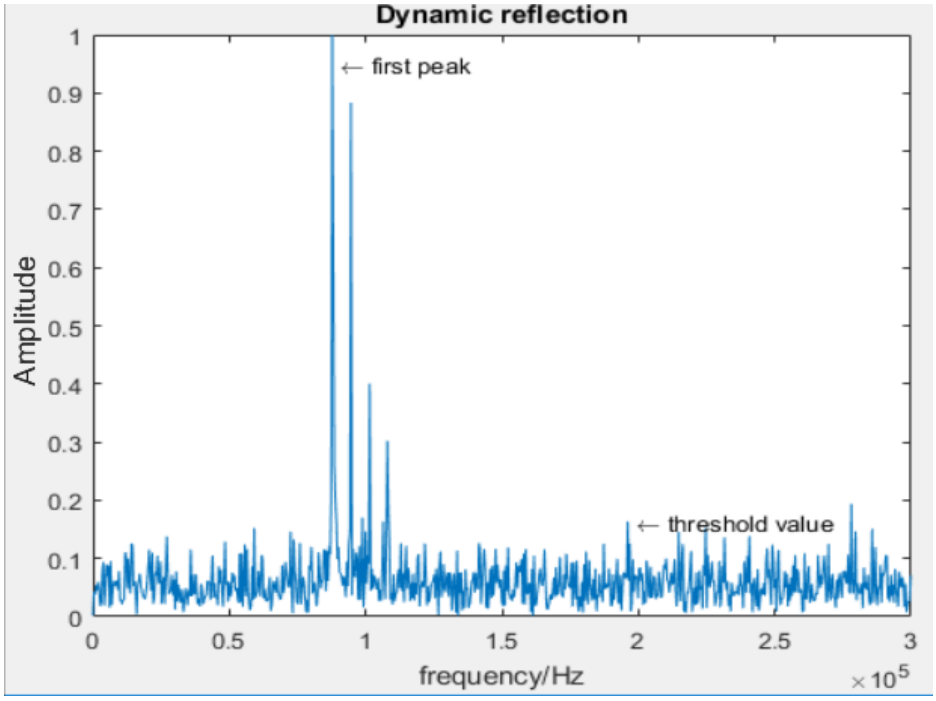

Figure 3-8. FFT results of dynamic reflections

3.4 Noise Mitigation Algorithms

As seen from Fig. 3-8, noises have appeared in the FFT frequency spectrum which can interfere the peak identification process. Like what has been developed for improving wireless communication performances, we will discuss the noise mitigation techniques to improve the tracking and location performances of the FMCW method.

3.4.1 Signal Averaging in Time Domain

The signal averaging algorithm utilizes the nature of randomness of noises and mitigate their effects by averaging them [31]. The detailed explanation is shown as:

Suppose that signal $y(t)$ contains two parts, a periodical signal $f(t)$ with a period of T_m and the random noise $n_y(t)$:

$$f[t-(i-1)T_m] = f(t)\ , \quad i = 1,2,3,...,N_s \quad . \tag{3-16}$$

Then, if $y(t)$ is repeatedly sampled N_s times with a period of T_m, the averaged signal of $y(t)$ is then:

$$\begin{aligned} \bar{y}(t) &= \frac{1}{N_s}\sum_{i=1}^{N_s}\{f[t-(i-1)T_m] + n_y[t-(i-1)T_m]\} \\ &= f(t) + \frac{1}{N_s}\sum_{i=1}^{N_s} n_y[t-(i-1)T_m] \end{aligned} \quad . \tag{3-17}$$

Then the signal-to-noise power ratio of the averaged signal is:

$$\begin{aligned} &\frac{E(|f(t)|^2)}{\frac{1}{N_s^2}E\{\sum_{i=1}^{N_s} n_y[t-(i-1)T_m]\}^2} = \frac{E(|f(t)|^2)}{\frac{1}{N_s^2}\sum_{i=1}^{N_s} E\{n_y[t-(i-1)T_m]\}^2} \\ &= \frac{E(|f(t)|^2)}{\frac{1}{N_s^2}N_s\sum_{i=1}^{N_s} E\{n_y(t)\}^2} = N_s\frac{E(|f(t)|^2)}{\sum_{i=1}^{N_s} E\{n_y(t)\}^2} \end{aligned} \quad . \tag{3-18}$$

The above equation shows that the signal-to-noise power ratio of the averaged signal is N_s times larger than that of the non-averaged signal. In terms of the signal-to-noise amplitude,

the improvement is $\sqrt{N_s}$ times. Note that $\frac{E(|f(t)|^2)}{\sum_{i=1}^{N_s} E\{n_y(t)\}^2}$ is the signal to noise power ratio of the non-averaged signal. During the derivation, we assume that the noise signals are un-correlated (e.g. Gaussian white noise) so that

$$E\{\sum_{i=1}^{N_s} n_y[t-(i-1)T_m]\}^2 = N_s \sum_{i=1}^{N_s} E\{n_y(t)\}^2 \quad , \qquad (3\text{-}18)$$

where E is the expectation operator. In addition, we assume that the target is not moving fast and remains static within the averaged time duration of $N_s T_m$; this will ensure the signals reflected from the target remain the same within $N_s T_m$. In our simulations, we chose N_s=9 and $N_s T_m$=0.1s.

Figure 3-9 presents the simulation results without the averaging while Figure 3-10 shows the results with the averaging.

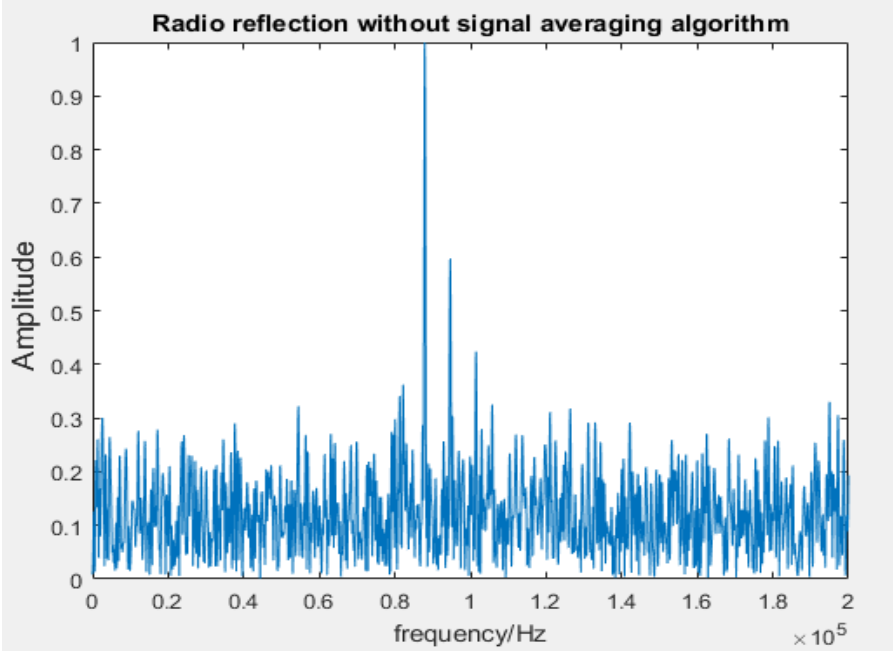

Figure 3-9. Dynamic reflections without the signal averaging

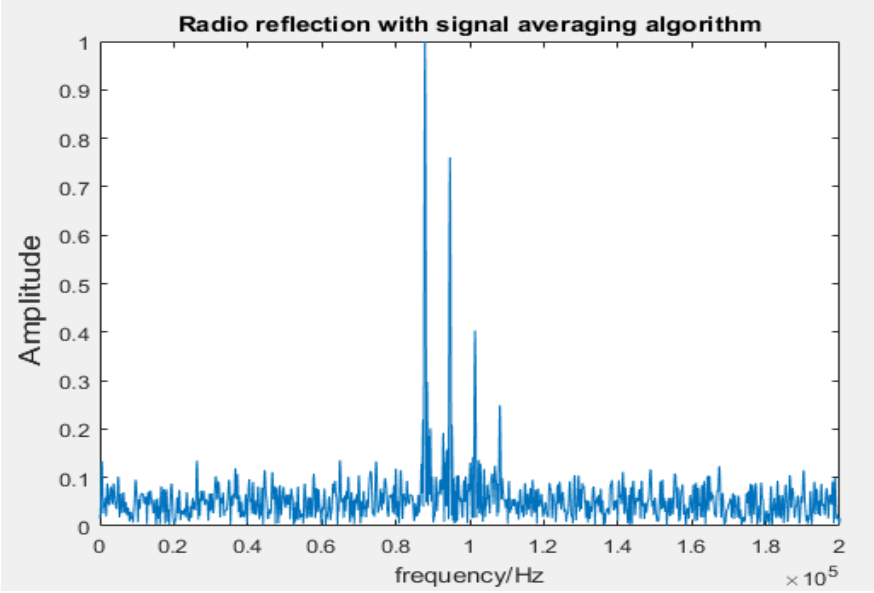

Figure 3-10. Dynamic reflections with the signal averaging

The comparisons of Fig. 3-9 and Fig. 3-10 shows clearly that with the averaging, the amplitudes of the signals reflected from the target stay unchanged; however, the amplitude of the noise has been significantly weakened. Since we averaged 9 times, the amplitude of the noise became approximately 3 times smaller than the original noise.

3.4.2 Other Advanced Noise Mitigation Techniques

Aside from the signal averaging algorithm, there are other advanced noise mitigation techniques, such as jump refection algorithm and Kalman Filter. The main idea of the former algorithm is to reject abnormal jumps of the target location. Since the target to be tracked is assumed to move at a relatively low speed, the tracking data about the target should be continuous between each FMCW sweep. Based on this fact, errors caused by the instantaneous strong noise or interference peaks can be removed. Similarly, based on the same fact, variation in the position of the target should stay smooth over time. As a result, a Kalman Filter can be used to smooth and enhance the distance estimation. We refer readers to [32] for more details.

3.5 Localization

The process discussed above allows us to determine the propagation delays and therefore the distances between a target and a FMCW transmitter/receiver system. It does not however give all the location information about a target such as the directions relative to

the transceiver. Therefore, more FMCW receivers are needed for obtaining the additional information. In the subsections below, we discuss about the way to locate a target still with the FMCW system.

3.5.1 Localization of a Target

For simplify and clarity, we consider first a two-dimensional case. To locate a target in the two-dimensional plane, at least two FMCW tracking receivers located at two different spatial positions are needed. As shown in Fig. 3-11, the ranges detected by two FMCW receivers can form possible positions of the target on an ellipse; therefore, intersections of two ellipses gives the precise location of the target [33].

Note that as shown in Fig. 3-11, the FMCW transmitting antenna and the two receiving antennas form the focus points of the two ellipses. In addition, in difference from the discussions before, the receiving and transmitting antennas are now located at two known but different locations from the transmitters. As a result, the distance we can calculate is the length of the path travelled by the signal, called the round trip distance (d1 or d2 shown in Fig. 3-11).

There is a possible ambiguity on where the location is above or below y=0 axis as shown in Fig. 3-11. Fortunately, most transmitting and receiving antennas have directional radiation patterns, which most likely make the signal strengths received from the target above and below y=0 very different; by using this fact, the ambiguity can be removed [13].

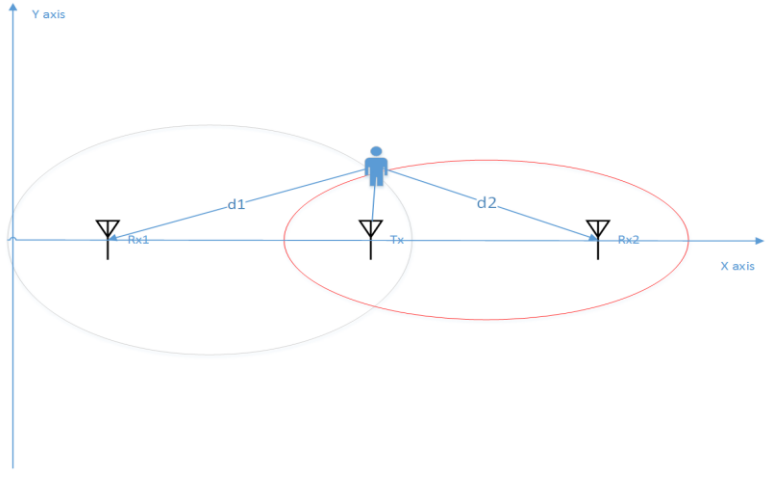

Figure 3-11. Two-dimensional localization

For three-dimensional location, a similar approach can be applied: we need to add one more receiving antenna and use three pairs of transmitting and receiving antennas to locate

the target by having three ellipsoids and determining its intersection point as the location of the target. Certainly, if more than three pairs of antennas are used, more information about the target position can be obtained and accuracy of the localization can be improved [14]. Since the principle for the three-dimensional location is similar to that for the two-dimensional, we will focus on the two-dimensional situation in this thesis and leave the three-dimensional case as one of the future work.

3.5.2 Simulation Results of the Two-dimensional Localization

In the following paragraphs, we present results of a two-dimensional example. The parameters used in the localization simulation are the same as those in Table 3-1, except that the location of the target moves from point (1, 9) to point (8, 2) over 14s, with the speed of $\frac{\sqrt{2}}{2}$ m/s. The transmitting antenna is located at point (5, 0) and two receiving antennas sit at point (0, 0) and point (10, 0) respectively. The simulation result is shown in Figure 3-12.

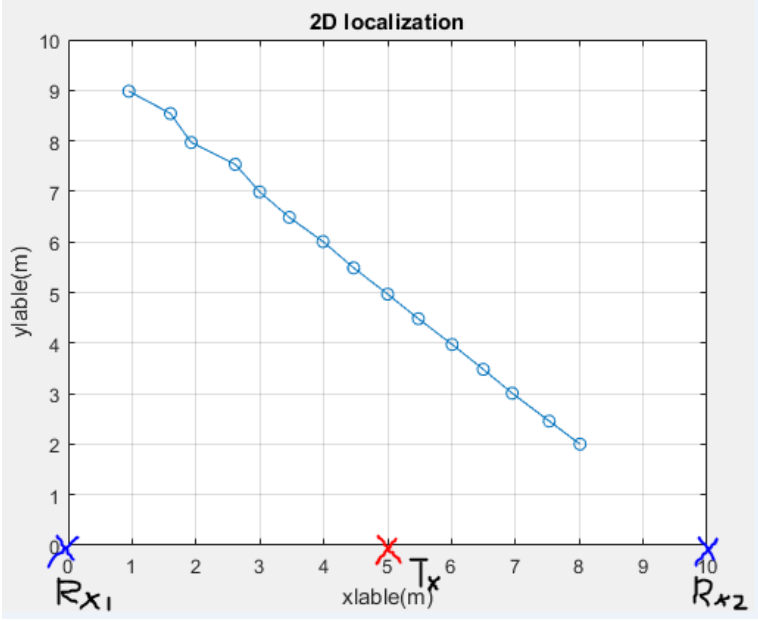

Figure 3-12. Simulation results of 2D localization with indoor FMCW radio tracking system.

As seen from the above figure, the tracking system works precisely and accurately.

CHAPTER 4 DETECTION METHODS USED IN THE INDOOR RADIO TRACKING SYSTEM AND THEIR PERFORMANCES

In this chapter, we focus on different detection methods used in the indoor radio tracking system. The first part of this chapter introduces and explains the basic idea of signal detection theory as well as the principle of constant false alarm rate (CFAR) detection. Then in the second part, the structure and mathematical model of the conventional detector of FMCW radar system is discussed. In the third part, a newly designed non-coherent detector of this FMCW radar system, which is based on forth order statistic, is illustrated and simulated in detail. Meanwhile, the parameters of this new proposed detector are also studied in this part. The fourth part introduces another non-coherent detection based on the third standardized moment. The final part compares the performance of these three detection methods under three different channels, AWGN, LOS and NLOS.

4.1 Background

4.1.1 Signal Detection Theory

Detection theory is a means to quantify the ability to discern between information-bearing patterns and random patterns that distract from the information [34]. In signal detection theory, the information-bearing patterns usually refer to the target signals and the random patterns represent the noise that exists in the channels, the electric circuits and devices.

The following figure is the model of binary signal detection [35].

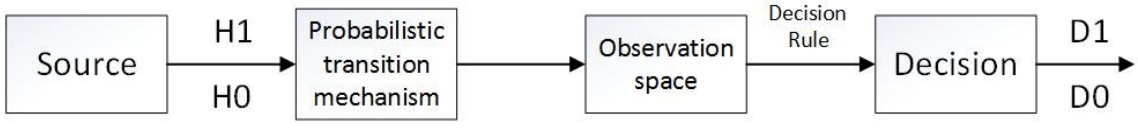

Figure 4-1. Model of binary signal detection

The source includes two different situations, hypothesis 1 (H_0) and hypothesis 2 (H_1) in signal detection theory.

The probabilistic transition mechanism maps the hypothesis of the source to a certain value, based on some probabilistic formula.

The observation space is a group that contains all the possible observations of the hypothesis generated by the source.

The decision rule (or criterion response) separates the whole observation space into two sub-spaces, D_0 and D_1. Samples located in a different sub-space are regarded as a different decision.

All the possible results of the binary signal detection are shown in Table 4-1.

Table 4-1. The decision results of binary signal detection

Hypothesis / Decision	H_0	H_1
D_0	P(D_0|H_0) (Correct rejection)	P(D_0|H_1) (Miss)
D_1	P(D_1|H_0) (False alarm)	P(D_1|H_1) (Hit)

Take a simple radar signal detection as an example. When there is no target within the range of the radar system, the received signal would only contain noise; otherwise, the signal captured by the receiving antenna would be a combination of both the noise and the radar signal. If we assume that the noise follows the Gaussian distribution and the signal we transmit is a constant signal with amplitude A, we have:

$$P(x \mid H_o) = \frac{1}{\sqrt{2\pi\sigma_n^2}} e^{-\frac{x^2}{2\sigma_n^2}} \quad , \tag{4-1}$$

$$P(x \mid H_1) = \frac{1}{\sqrt{2\pi\sigma_n^2}} e^{-\frac{(x+A)^2}{2\sigma_n^2}} \quad , \tag{4-2}$$

where σ_n is variance of the noise, and A is the amplitude of the signal.

To make the above easy to understand, Figure 4-2 provides a direct visual graph of the entire process of signal detection. The x axis represents the entire observation space. The signal and noise are mapped to samples inside the observation space, following its own

probability design distribution. The criterion separates the graph into 4 parts, Correct Rejections, Miss, False Alarm, and Hit. Each condition is defined in Table 4-1. More specifically, the Correct Rejections represents the probability that detection can correctly filter the background noise. The Hit refers to the ability that detection can correctly detect a target signal. In contrast, the False Alarm is the case when the detection mistakes the noise for the desired signal, while the Miss demonstrates the probability when the signal is too weak to be detected by the proposed criterion. Therefore, the ability to correctly detect a target signal (correct detection probability) can be defined as:

$$P_d = P(D_1 \mid H_1) - P(D_0 \mid H_1) \tag{4-3}$$

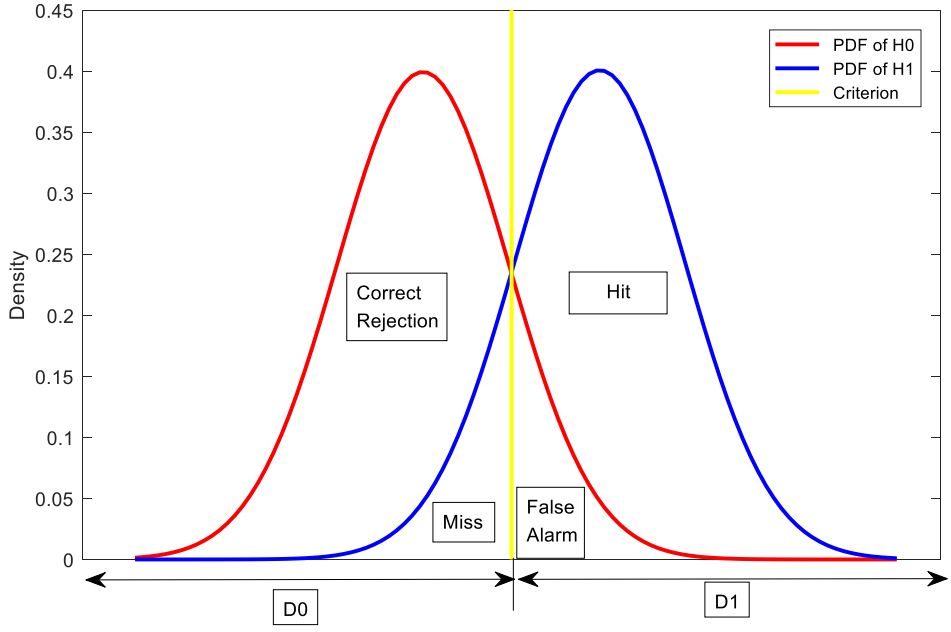

Figure 4-2. Four possible results of the binary signal detection

As seen from Figure 4-2, the position of the criterion (or in other words, the value of the threshold) plays an important role in the performance of the detection, since it may influence the four probabilities in Table 4-1 directly. There are several well-known theories about how to set an optimum threshold, e.g., Bayes Criterion. We refer the reader to [36] for more details. In our simulation, a CFAR method is used to design our detection, which will be discussed in section 4.1.2. In order to obtain a better performance of the detection, the structures or parameters of our detection can be changed to decrease the overlap of the distribution probability of signal and the noise. An example is provided in section 4.3.5.

4.1.2 Constant False Alarm Rate (CFAR) Detection

Due to uncertainties of the environment, such as background noise, using a fixed criterion detection may weaken the detection performance significantly. It is quite possible that at a time, the noise in the channel is relatively weak. However, in the next moment, the background noise may become quite strong because of some unexpected occurrences happened in the channel. In this situation, a fixed criterion detection may result in a dramatic increase of the false alarm rate, and hence, the correct detection probability will degrade sharply.

To fix this problem, instead of using a fixed threshold detection, engineers prefer to use a detection called constant false alarm rate (CFAR) detection, which can maximum the detection performance of the system while maintaining a constant false alarm rate in the noise environment [37]. In other words, the threshold of the CFAR detection is no longer a fixed value, it can change itself based on the power of the background noise that exists in the channel to maintain a constant false alarm rate. Therefore, the variations in the environment characteristics, such as noise, will not have a significantly harmful effect on the detection performance.

The design process of constant false alarm rate detection can be described as follows:

1. Setting up a mathematical model of the input of the detection.

2. Figuring out the probability density function of the interference factor (noise) using the background information.

3. Calculating the threshold of the detection, based on the probability density function (PDF) of the noise and the given false alarm rate.

4. (Optional) Calculating the theoretical detection probability from the threshold and the PDF of the received signal.

4.2 The Conventional Constant False Alarm Rate (CFAR) Detection in the Indoor Radio Tracking System

As described in Chapter 3, after the channel, the received signals are a combination of unpredictable echoes or reflected signals traversing through different paths. Even after the background subtraction, there are still many reflected signals caused by the target itself, called dynamic reflections. Therefore, the mathematical model of the signals we need to process at the detection can be expressed by having multiple copies of signal (3-14) with different beat frequencies and delays:

$$y(t) = \sum_{i=1}^{M} y_i(t) + n(t) \quad , \tag{4-4}$$

$$y_i(t) = \sqrt{2p_{y_i}} \cos(2\pi f_{beat,i} t + 2\pi f_c \tau_i - \pi \frac{B}{T_m} \tau_i^2) \quad . \tag{4-5}$$

Here $y_i(t)$ is one of the dynamic reflections captured by the receiving antenna and processed by the indoor FMCW system, M is the number of dynamic reflections, τ_i is the propagation delay of the ith dynamic reflection, $f_{beat,i} = \frac{B\tau_i}{T_m}$ is the beat frequency of the ith dynamic reflection, and $n(t) = \sum_{i=1}^{M} n_{y,i}(t)$ is the total background noise in the system.

Based on section 3.3, the dynamic reflections can be solved by knowing that the signal with the smallest frequency shift represents the directly reflected signal of the target. Therefore, after the signal is transformed from time domain to frequency domain by FFT, an appropriate threshold can be set using the theory of CFAR detection, and the first signal peak that is larger than the threshold in the frequency domain can be identified. Then its corresponding frequency can be used to calculate the TOF of the FMCW signal. In other words, the directly reflected signal can be separated out of the rest dynamic reflections.

Therefore, to make the discussion and mathematical derivation clear and easy to understand, in the following section, we focus on the directly reflected signal only and neglect the other directly reflected signals or multi-path effects. As a result, the signal model is simplified as:

$$y(t) = \sqrt{2p_y}\cos(2\pi f_{beat}t + 2\pi f_c\tau - \pi\frac{B}{T_m}\tau^2) + n_y(t) \quad (4\text{-}6)$$

The first part of the equation is generated by a directly reflected signal whose frequency contains the information of the propagation delay τ. The rest part is the background noise.

In the following subsections, we will discuss the CFAR detection.

4.2.1 Structure and Principle of Conventional CFAR Detection

Figure 4-3 shows the structure of a conventional CFAR detection without considering multipath effects of the channel. The input signal is shown in Equation (4-6). After the FFT, the signal is shown in Figure 4-4. Our objective is to find the signal peak and use its corresponding frequency to calculate the propagation delay and hence to locate the target. For the conventional CFAR detection, it uses a straightforward decision method: setting an appropriate threshold based on the desired false alarm rate (FAR) and the power of the noise; the first frequency bin whose value is larger than the threshold is regarded as the bear frequency of the target [19].

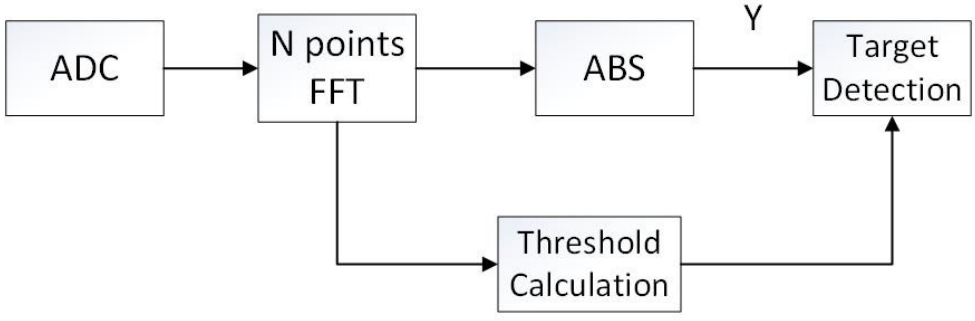

Figure 4-3. The structure of the conventional CFAR detection

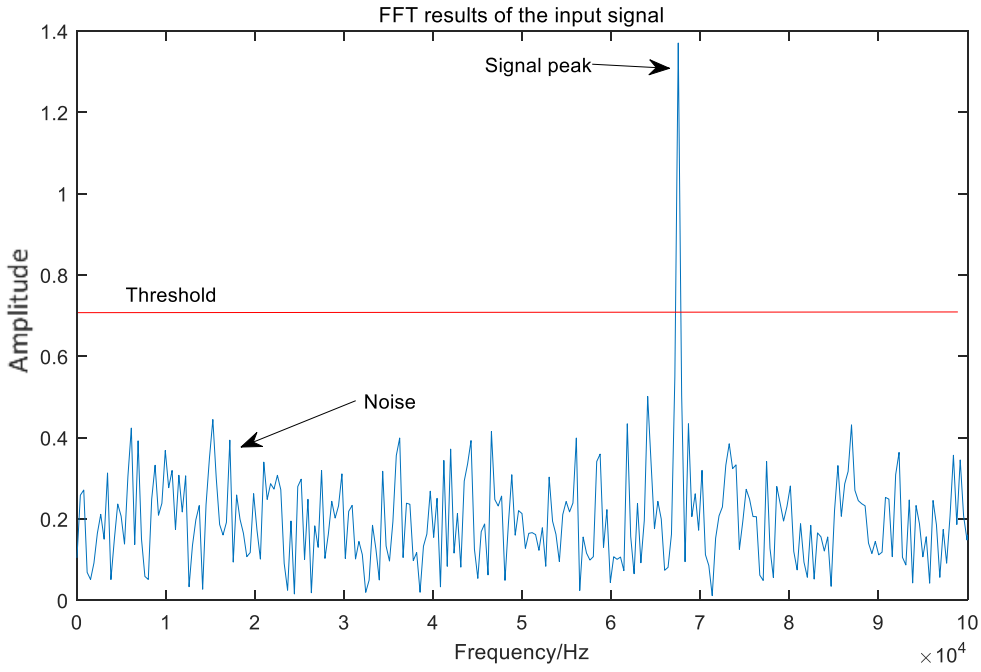

Figure 4-4. FFT results of the input signal

From Figure 3-4, we can see that the N_{FFT} point FFT is applied to the signal $y(t)$ after ADC. Thus, the whole pass-band of the low-pass filter, $BW_{\text{low-pass,}}$ has been divided into N frequency bins and the target detection is conducted at each independent frequency bin. For each frequency bin (denoted as f_{bin}), there are only two situations: the bin that contains both the signal and the noise or the bin that includes only the noise. Mathematically, the frequency-domain output is:

$$H_o: \quad Y_n \qquad \text{at } f_{bin} \qquad \text{(no target signal)}, \tag{4-7}$$

$$H_1: \quad Y_n + Y_s \qquad \text{at } f_{bin} \qquad \text{(target signal is present)}, \tag{4-8}$$

where Y_n is the FFT result of the white Gaussian noise and Y_s is the FFT result of the reflected signal.

Since we assume that the time-domain thermal noise is the circularly symmetrical complex Gaussian noise with an average power calculated as $N_o \cdot BW_{low-pass}$ in the MATLAB simulation, where N_0 is the power spectral density of the thermal noise and $BW_{low-pass}$ is the pass-band of the low-pass filter. It can be shown that H_o follow Rayleigh distribution as [19]:

$$f(Y_n) = \frac{Y_n}{\sigma^2_{n\_bin}} e^{-\frac{Y_n^2}{2\sigma^2_{n\_bin}}} \quad , \tag{4-8}$$

where

$$\sigma^2_{n\_bin} = \frac{\sigma^2_n}{N_{\text{FFT}}} = \frac{N_o \cdot BW_{low\_pass}}{N_{\text{FFT}}} \tag{4-9}$$

is the average power of the noise in one frequency bin and N_{FFT} is the number of FFT points used.

With CFAR detection, the value of the threshold (Y_{th}) for a given false alarm rate is defined as follow:

$$P(Y_n > Y_{th}) = FAR \ (specified) \tag{4-10}$$

Or,

$$\int_{Y_{th}}^{\infty} \frac{Y_n}{\sigma^2_{n\_bin}} e^{-\frac{Y_n^2}{2\sigma^2_{n\_bin}}} dY_n = FAR \tag{4-11}$$

It leads to:

$$Y_{th} = \sqrt{-2\sigma^2_{n\_bin} \ln(FAR)} \tag{4-12}$$

As seen, threshold value Y_{th} is determined by a given or specified FAR and average power $\sigma^2_{n\_bin}$ of the noise in one frequency bin.

The decision is then made with the following formulas:

$$Decision = \begin{cases} D_o & \text{when } Y_n \le Y_{th} \\ D_1 & \text{when } Y_n > Y_{th} \end{cases} \quad . \tag{4-13}$$

4.2.2 Simulation Results of the Conventional CFAR Detection Under Different Channels

Based on the discussion above, we run the simulations of the FMCW system with the CFAR detection technique and then assess the performances. There are two ways to quantify the performances. One is to simulate detection probability versus signal to noise ratio. Another is to measure the so-called mean absolute error (MAE), which is defined as :

$$MAE = \frac{1}{N_e}\sum_{n=1}^{N_e}\left|\tau - \hat{\tau}_n\right| \quad , \tag{4-14}$$

where N_e is the number of the TOA estimates conducted. τ is the real TOA for the target, and $\hat{\tau}_n$ is the nth estimated TOA. MAE is essentially the approximating the mean error between the real TOF and the estimated TOA.

The following two figures show the detection probability and MAE with different E_p/N_0 respectfully. The parameters used in the simulation are listed in Table 4-2.

Table 4-2. Parameters Used in the Conventional CFAR Detection Simulation

Parameters	Value	Parameters	Value
fc (GHz)	5.56	F_s (GHz)	20
Tm(ms)	2.5	N_{FFT}	250000
B(GHz)	1.69	$BW_{\text{high-pass}}$ (GHz)	5
d(m)	15	$BW_{\text{low-pass}}$ (KHz)	300
Down-sampling rate	200	Channel Type	AWGN,LOS, NLOS

Here f_c is the initial carrier frequency of the FMCW signal, T_m is the chirp duration, B is the maximum frequency shift of the FMCW signal in one sweep, d is the distance between the target and antennas. $d_{\max}$ is the max range of the tracking system, F_s is the sampling rate used in the MATLAB simulation. N_{FFT} is the FFT points used in the system. $BW_{\text{low-pass}}$ is the passband of the low-pass filter. $BW_{\text{high-pass}}$ is the passband of the high-pass filter. Down-sampling rate is the ratio between the sampling rate we used before the ADC and the real sampling rate we used after the ADC. The reason why we need to down-sample the sampling rate has been explained in section 3.3.3. Three different channels are used for the simulations: AWGN, 802.15.4a CM3 (LOS) and 802.15.4a CM4 (NLOS). Fig. 4-5 and Fig. 4-6 show the simulation results.

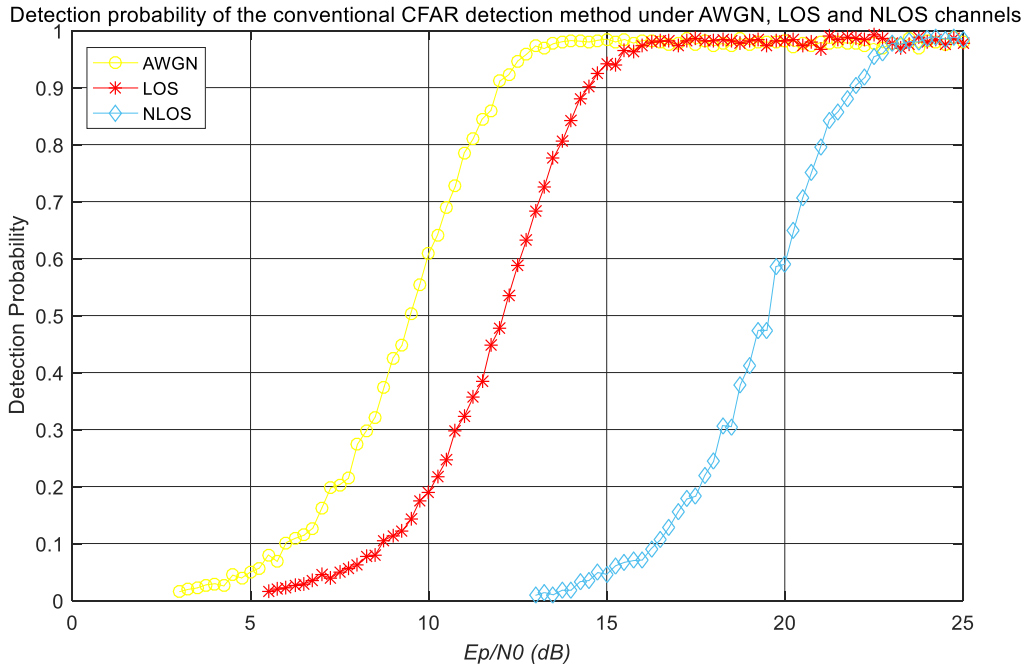

Figure 4-5. Detection probability of the conventional CFAR detection method under AWGN, LOS and NLOS channels

As can be seen from Figure 4-5, all these three curves follow the same trend, indicating that the detection probability becomes higher with the increase of signal to noise ratio under the three channel conditions. However, under AWGN, the detection probability starts to climb first and levels off at the E_p/N_0 of 13dB; the detection probability funder LOS levels off at at the E_p/N_0 of 16dB; the detection probability under NLOS level's off at at the E_p/N_0 of 23dB. The results are expected since the AWGN channel does not have the multipaths while NLOS channel is rich of multi-path reflections. Interestingly, all three channels present the same maximum detection probability of 98.2%. This is because the total processing time of the conventional detection can be calculated as:

$$T_d = T_s \cdot P_t \quad , \tag{4-15}$$

where T_s is the simulation time for one specific E_p/N_0. In our simulation, for each E_p/N_0, we conduct 2000 MATLAB simulations and use their average value as our simulation results. P_t is the position of the FFT bin caused by the target. Using the parameters in Table 4-2, P_t is 170. Hence, the theoretical detection probability can be calculated as:

$$P_d = 1 - \frac{T_d \cdot FAR}{T_s} = 98.3\% \quad , \tag{4-16}$$

which is agreeable with the simulation results obtained.

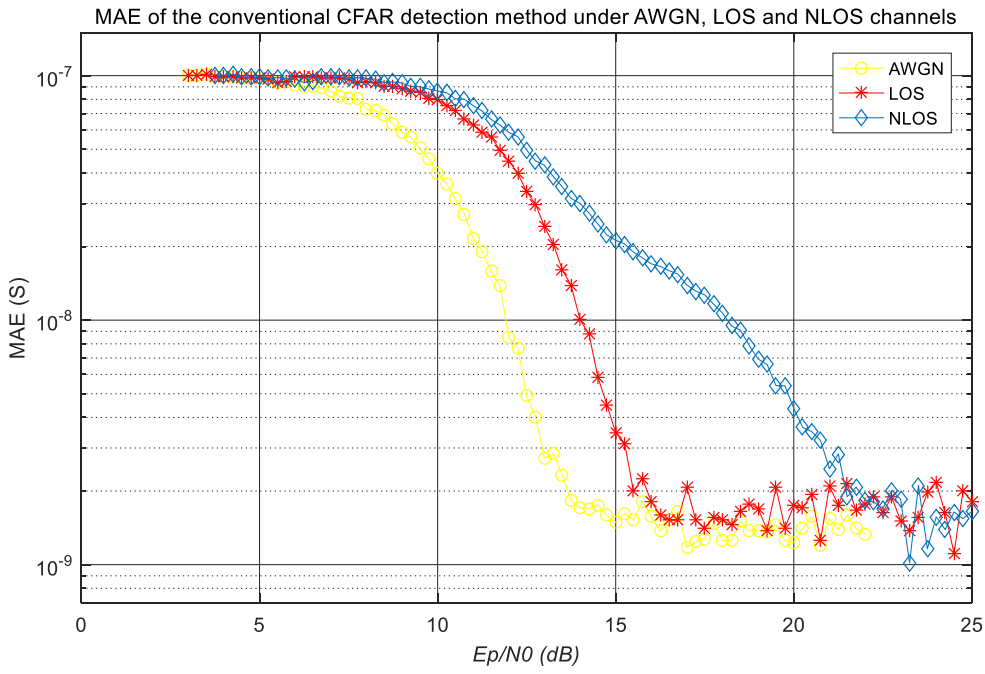

Figure 4-6. MAE of the conventional CFAR detection method under AWGN, LOS and NLOS channels

Figure 4-6 presents the same conclusions as Figure 4-5: with the increase of signal to noise ratio, the MAE of the TOF becomes smaller and smaller. Also, for a signal-to-noise ratio of 5 dB to 22 dB, AWGN channel presents the smallest MAE while the NLOS channel gives the largest MAE, indicating that the CFAR has the best performance under AWGN and the worst performance under NLOS.

Interestingly, the MAE curve under NLOS is different from those under AGWN and LOD: it seems to have a plateau when the SNR is around 15 and 16dB. This phenomenon can be explained as follows. Before this plateau, the signal-to-noise ratio is relatively small so the most likely signal for the system to detect is the strongest reflected signal, as shown in Fig. 4-7. With larger and larger signal-to-noise ratio, the threshold of CFAR detection becomes lower and lower (i.e. the red horizontal line in Fig. 4-7 is lower and lower); hence it becomes possible that the second strongest reflected signal is detected. When the signal-to-noise ratio is within a region of 15dB to 16 dB, the detector may mistakes the second strongest peak as the target impulse. As a result, the MAE keeps constant in this region. With the signal-to-noise ratio continuing to increase, the detector begins to detect the target impulse successfully again. When the signal-to-noise ratio increases to 23 dB, all MAEs level off at its minimum of slightly higher than 10^{-9}s.

On the other hand, when the signal-to-noise ratio is low, e.g., smaller than 5 dB, the MAEs under all three channel conditions remain at 10^{-7}s; this is because the estimated TOF is

considered as 0s when there no peak value is larger than the threshold (indicating that all of the signals have been inundated by the noise). In this situation, the MAE will be calculated as:

$$MAE = (\tau - \hat{\tau}_n) = \tau = \frac{2d}{c} = 10^{-7} \quad , \tag{4-17}$$

where d is the distance between the target and the antennas and c is the speed of light.

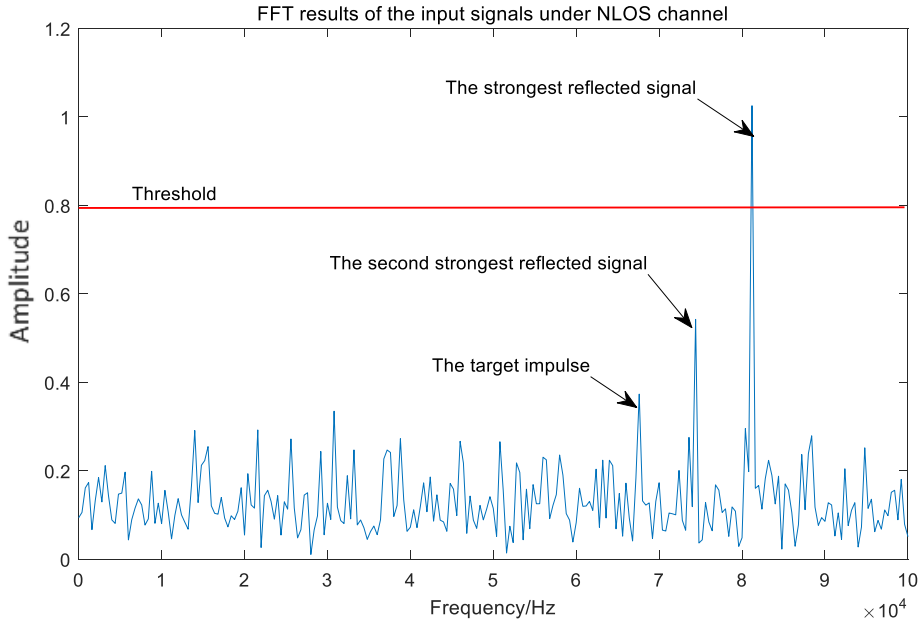

Figure 4-7. FFT results of the input signals under the NLOS channel

4.3 The Proposed Kurtosis Detection in the Indoor Radio Tracking System

In the previous section, we discussed the principle and structure of the conventional CFAR detector used in the indoor FMCW radio tracking system. Such detection does have some advantages; for example, it has simple structures so that it is able to be implemented in practice. Besides, it also has low power consumption because of its characteristics of non-coherent detection. However, such advantages are achieved at the expense of some loss of performances. Therefore, we propose a new non-coherent detection, based on the fourth

order statistic, i.e., Kurtosis, which has a higher detection probability than the conventional detection within a moderate signal-to-noise region.

The organization of this section is as follow. First, we present the definition of Kurtosis and how it could be used to help enhance the performance of detection. Then, the structure and implementation of Kurtosis detector is shown. Next, we apply a classic mathematical method into the Kurtosis detection to improve its efficiency. Then we show how to estimate a specific threshold for the Kurtosis CFAR detection. The final part contains two topics, the first one is the parameters study which explains how the different parameters influence the performance of the Kurtosis detector. The other shows the performance evaluation of the Kurtosis detector under different channels, including AWGN, LOS and NLOS channels.

4.3.1 Fourth Order Statistic - Kurtosis

The Kurtosis, which is also called as the fourth order statistic, is a statistical quantity for indicating the difference between a random variable and a Gaussian random variable [38]. Its definition is:

$$kurt(x) = \frac{E[(x-u)^4]}{\{E[(x-u)^2]\}^2} \quad , \tag{4-18}$$

where $\mathrm{E}\{.\}$ represents the expectation operator and u is the mean of the variable x.

For N_{sa} limited samples of x, its kurtosis value can be estimated as:

$$kurt(x) \approx \frac{\frac{1}{N_{sa}}\sum_{i=1}^{N_{sa}}(x_i-\bar{x})^4}{\{\frac{1}{N_{sa}}\sum_{i=1}^{N_{sa}}(x_i-\bar{x})^2\}^2} \quad , \tag{4-19}$$

where $\bar{x}$ is the average of the sample values.

According to [39], the kurtosis value for a Gaussian random variable is 3. Thus, if the kurtosis result for a random variable is larger than 3, it means that such variable follows a distribution which has sharp peaks and longer tails than the Gaussian random variable. In other words, the kurtosis value actually describes the extent to which a random variable deviates from a Gaussian random variable.

In our situation, as mentioned before, the frequency bin that contains only the noise follows the Rayleigh distribution. Thus, when a window is designed in the frequency domain and the kurtosis value is calculated for the samples inside the window, if all the samples are caused by noise, the kurtosis value will be slightly higher than the Gaussian distribution: it was found to be around 3.2 by MATLAB simulations. This is because FFT results of noise follow a Rayleigh distribution and the Rayleigh distribution has a similar smooth shape with the Gaussian distribution. Therefore, the kurtosis value is just slightly larger than 3. However, when the window includes both the signal and noise, its kurtosis value will be much greater than 3 due to the impulsive nature of the signal. Hence, we could use this characteristic to detect the target signal.

4.3.2 The Structure and Working Process of Kurtosis Detection

The structure of the proposed Kurtosis detection has been shown in |Figure 4-8. Compared with the conventional detection we mentioned before, there are two extra modules in Kurtosis detection, the register module and the shift window module.

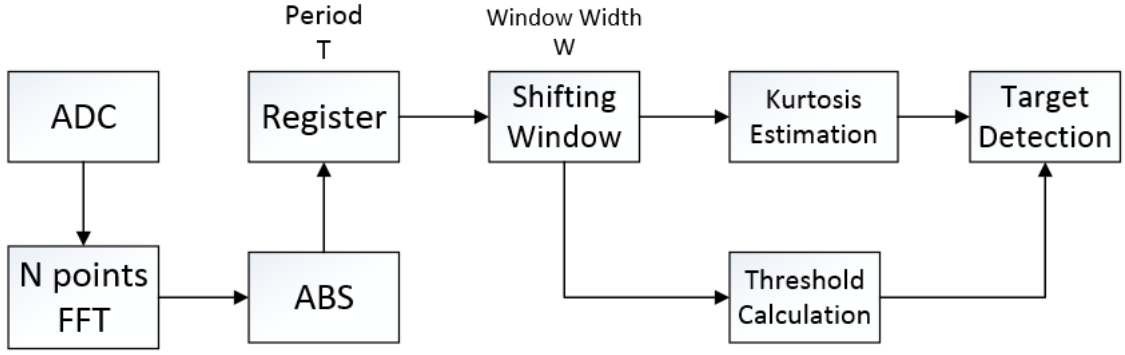

Figure 4-8. The structure of the proposed Kurtosis CFAR detection

As defined by Equation 4-18, the Kurtosis is a statistic component and hence requires enough samples to calculate; otherwise, the errors will be large. As a result, we use a register module to collect enough samples for Kurtosis calculation. Specifically, we save T sets of entire FFT data (for more details about how to obtain the FFT data is described in Chapter 3) for the future processing by the register module.

Since the target we want to track in the FMCW tracking system is often a human, whose speed is not too fast, within a relatively short period, say 20 (T=20) times duration of the chirp signal ($T \cdot T_m = 20 \times 2.5 \times 10^{-3} s = 0.05 s$), the position of the target stays unchanged. Thus, in these 20 sets of FFT data, the signal peaks caused by the target are all at the same

position in the frequency domain because they all have the same frequency shift. The only difference between these 20 sets of FFT results is the amplitude of the signal peak because the white Gaussian noise changes instantaneously in this short term. As shown in Figure 4-9, there are T sets of different FFT outputs, each of which has a different shape and amplitude because of the instantaneous background noise. However, one important fact is that the FFT bins which contain the target signal (signal peak marked in the figure) are all located at the same position, which is around 6.8×10^4 Hz, indicating that the location of the target is unchanged within this processing time ($T \cdot T_m$).

After we saved the T times FFT outputs, we can set a window whose width is W points for each of these T sets of FFT outputs at the beginning of the frequency axis (the red window shown in Figure 4-9). Then we merge all of these T windows into a new larger window whose points become $W \cdot T$. If there is no signal pulse in the window, for example, the red window or the green window in Figure 4-9, the kurtosis value of all the FFT bins (points) inside that window will be around 3.2; this is because all the FFT bins (points) are caused by the white Gaussian noise which follows a Rayleigh distribution. Then we shift the window one point to the right and repeat the merge and kurtosis calculation. Once the window first reaches the signal pulse (the brown window in Figure 4-9), the kurtosis result will jump to a much larger value than 3.2 and the reflection from the target is then identified.

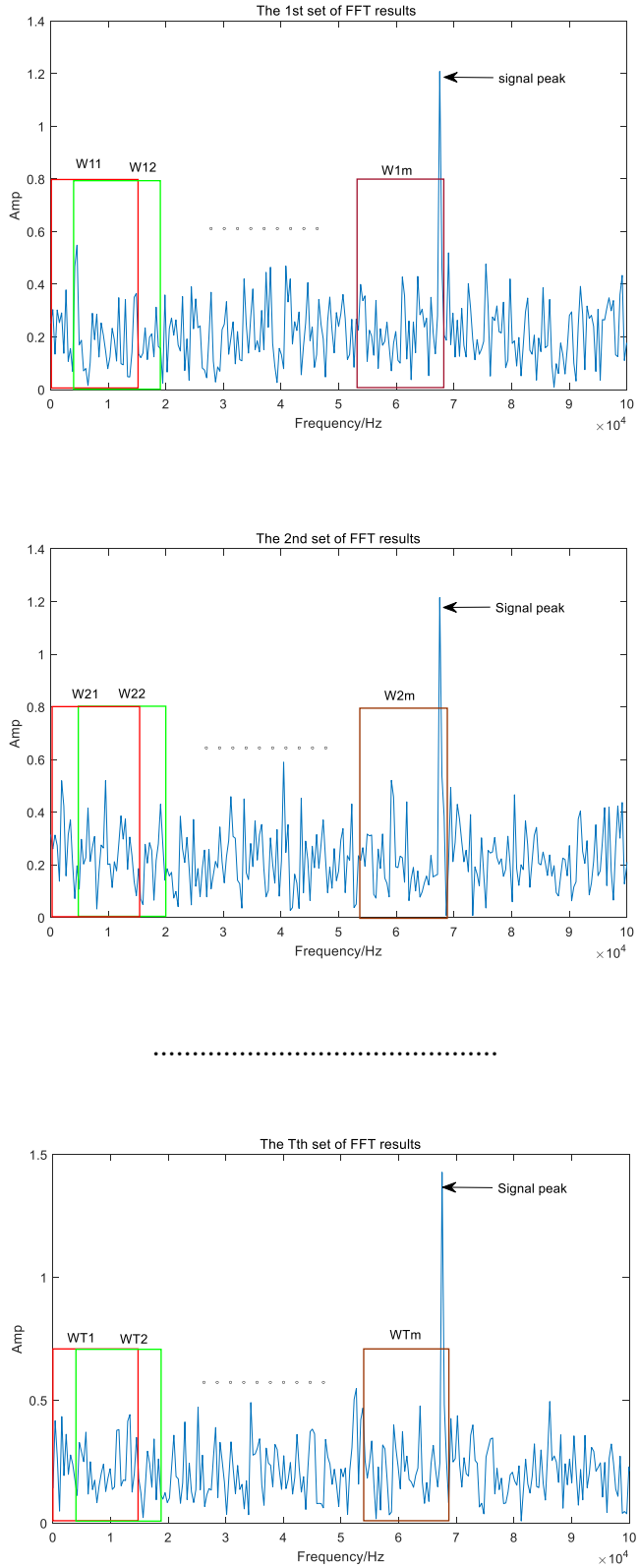

Figure 4-9. The exhibition of *T* sets of FFT results and its window shifting process

The above window shifting process is carried out and the results are shown Fig. 4-10. The simulation parameters presented in Table 4-3.

Table 4-3. Parameters Used in the Kurtosis CFAR Detection Simulation

Parameters	Value	Parameters	Value
f_c (GHz)	5.56	F_s (GHz)	20
T_m(ms)	2.5	E_p/N_0 (dB)	15
B(GHz)	1.69	N_{FFT}	250000
d(m)	15.0	$BW_{\text{low-pass}}$ (KHz)	300
Down-sampling rate	200	$BW_{\text{high-pass}}$ (GHz)	5.0
T	20	W	50

where f_c is the initial carrier frequency of the FMCW radar signal, T_m is the chirp duration. B is the maximum frequency shift of the FMCW signal in one sweep. d is the distance between the target and antennas. $d_{\max}$ is the max range of the tracking system. F_s is the sampling rate used in the MATLAB simulation. Signal to Noise Ratio is 15 dB. N_{FFT} is the FFT points used in the system. $BW_{\text{low-pass}}$ is the passband of the low-pass filter. $BW_{\text{high-pass}}$ is the passband of the high-pass filter. T is the period used in the register module. W is the width of the shifting window. Down-sampling rate is the ratio between the sampling rate used before the ADC and the sampling rate used after the ADC. The reason to down-sample the sampling rate is explained in section 3.3.3.

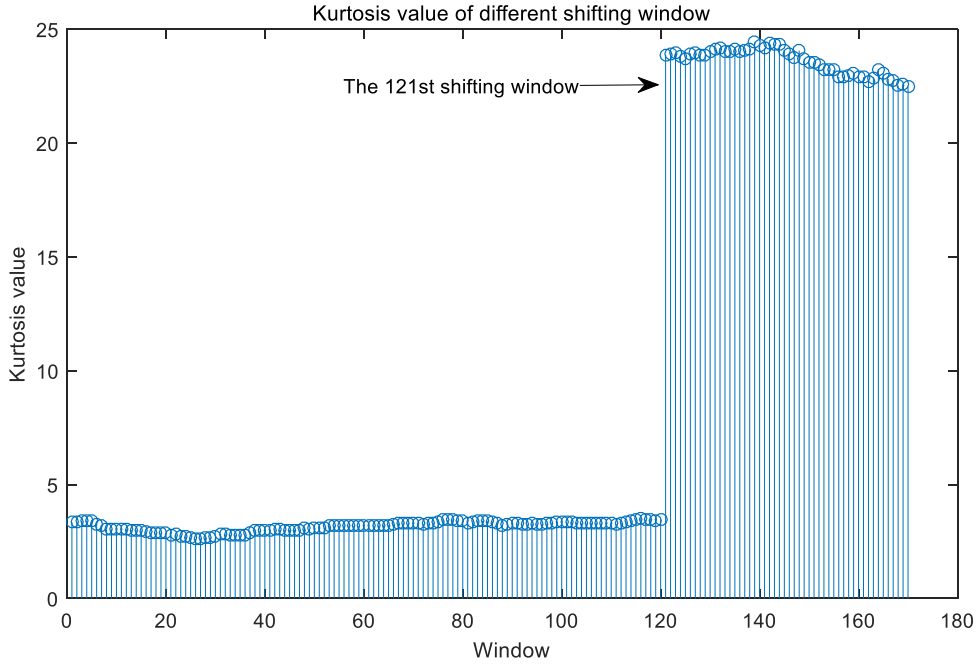

Figure 4-10. Kurtosis value of different shifting windows

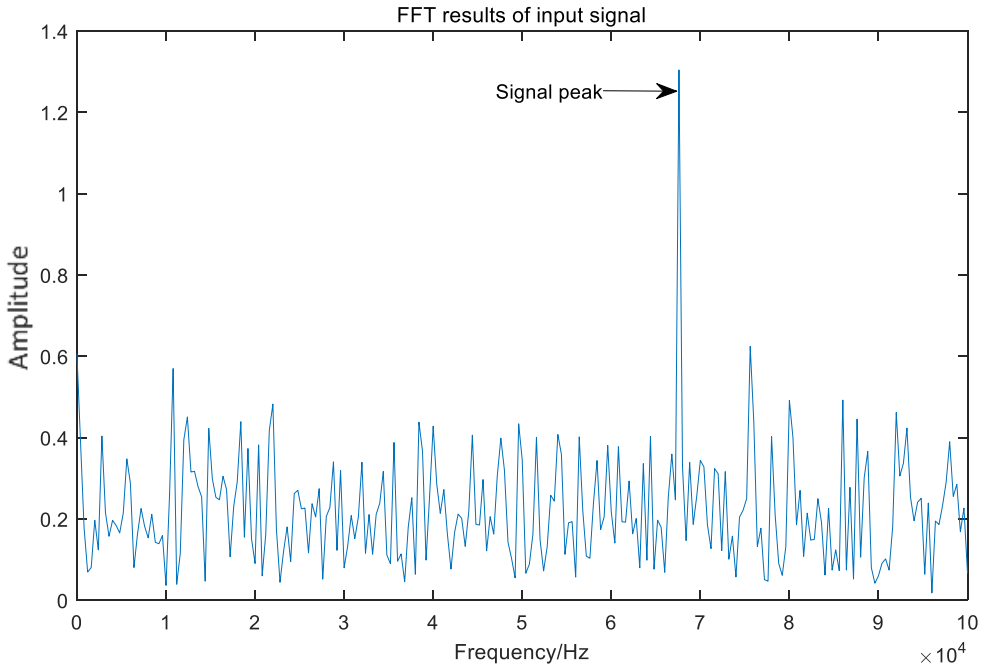

Figure 4-11. FFT results of input signal of Kurtosis detection in one period processing

In Fig. 4-10 shows the Kurtosis values when the window is moved from the beginning to the 170th window point by point. the Kurtosis value has a big jump at the 121st window, indicating that this particular window, which is written as W_{target}, is the first shifting window that contains the target signal. Thus, the FFT bin located at the right edge of the 121st window is the signal peak we are looking for. It corresponds to the peak of the FFT results shown in Fig. 4-11. Then, the location of the target can be calculated as follows:

The size of one bin of the FFT Δf_{min} is:

$$\Delta f_{\min} = \frac{Bandwidth}{N_{FFT}} = \frac{F_s}{(down\ samplifing\ rate)\cdot N_{FFT}} = 400Hz \quad . \tag{4-20}$$

Therefore, the beat frequency f_{beat} for the signal directly reflected from the target can be obtained as:

$$f_{beat} = (W_{target} + W - 1)\Delta f_{\min} \quad . \tag{4-21}$$

In the above example, W_{target} is found to be 121; thus, the beat frequency is equal to 68kHz.

Based on Chapter 3, the propagation delay τ and the distance d could be obtained as:

$$\tau = \frac{f_{beat} T_m}{B} = 100.6\ (ns) \quad , \tag{4-22}$$

$$d = \frac{c\tau}{2} = 15.08\ (m) \tag{4-23}$$

The distance d is 15.08 m. The error is 8 cm, which meets the requirement of the FMCW resolution discussed in section 3.1.3.

Besides, comparing the two figures above, it is not hard to notice that after doing the Kurtosis calculation, the gap between the signal FFT bin and the noise FFT bin becomes significantly wide. In other words, it becomes much easier to distinguish the signal peak from the background noise. Hence, we could conjecture that the performance of Kurtosis detection is better than the conventional detection within certain SNR regions.

4.3.3. Bisection Method in Shifting Window

In the previous section, we have discussed the working process of the Kurtosis detection, including how to use register and save enough samples and how the shifting window module finds the target impulse. However, one obvious drawback is that it requires enormous calculations to find the target impulse because it must shift and calculate the Kurtosis value for each shifting window point by point. Such a process is time-consuming and unnecessary. Therefore, simple methods are much desirable, e.g., Bisection method, which is also called Binary Search Method in some papers [40].

The bisection Method in mathematics is a root-finding method that repeatedly bisects an interval and then selects a sub-interval in which a root must lie for future processing [41]. According to this definition, we can re-design our window shifting algorithm more efficiently as follow.

At first, we set an initial window at the origin as the current window, with window width *W*. Since there is no target impulse in this initial window (the reason will be explained in section 4.3.5.1), we shift this window to the right with *W* points and get a new current window. We calculate its Kurtosis value again. If the Kurtosis value is not larger than the threshold, there is still no target impulse in the current window; otherwise, there must be some peaks caused by the target. When the Kurtosis value is larger than the threshold value, we consider the current window as the initial interval and apply the bisection method at this point. Just as defined in [41]. The bisection algorithm is a loop and for each loop the algorithm evenly separates the interval into two parts, the left and right. For each part, we

still set a window of which the width is equal to W and calculate its corresponding Kurtosis value. For the part that contains the target impulse, its Kurtosis value will be much larger than the threshold due to the signal impulse natures, while the other part which only includes the noise FFT will not exceed the threshold. As a result, we could identify the correct part that contains the target impulse in this way and use it as our new interval. We keep doing this loop until the interval is too small to be separated. At this point, we can locate the position of the target FFT bin and use its frequency to calculate the TOF.

In a multi-path situation with dynamic reflections, it is quite possible that both the left and right windows contain the target impulses, causing both of their Kurtosis results to be larger than the threshold. In this case, no matter how many target impulses there are in the frequency domain, the directly reflected signal will have the smallest beat frequency. It will stand in the far left position in the frequency domain. Hence, if both left and right windows' Kurtosis value exceed the threshold, the directly reflected signal should be located in the left side; we update the left part as our new interval and do the bisection algorithm again until the accurate position of the target impulse is found. By using this algorithm, the time and calculations of the shifting window process has been significantly reduced. In the following simulations, we choose to use this novel algorithm rather than the original one. Fig. 4-12 shows the flow chart of the bisection method.

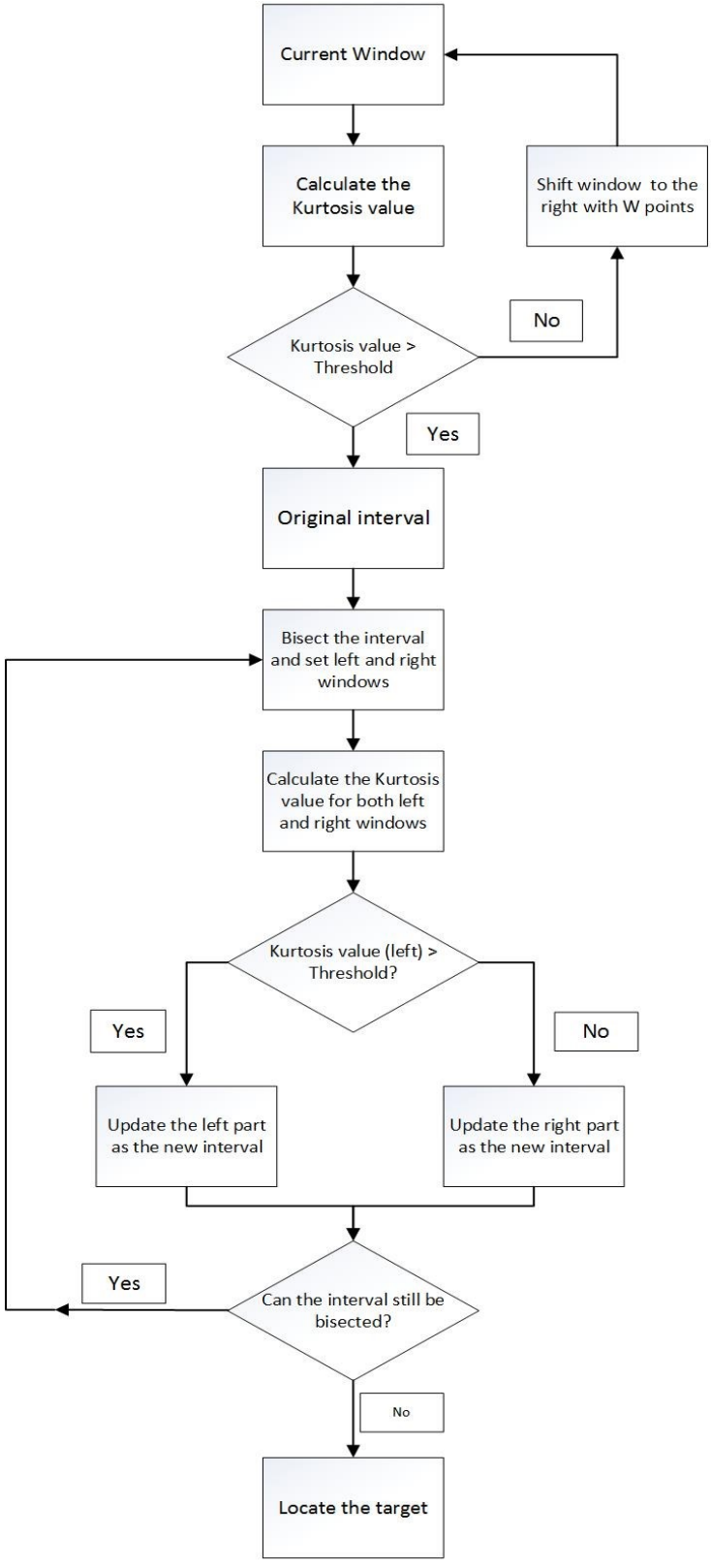

Figure 4-12. The flow chart of the Bisection method

4.3.4 The Threshold Value for the Kurtosis Detection

After we have obtained the Kurtosis value of different shifting windows as shown in Figure 4-10. In order to let this method work, similarly to the conventional method, an appropriate threshold need to be set. Again, the CFAR operation can be applied. In difference from the CFAR for the conventional method, the binary hypothesis is no longer the FFT outputs caused by noise but the Kurtosis results of the window that contains only the noise and the Kurtosis results of the window that includes both the signal and the noise. Mathematically, they are:

$$H_o: \quad K = kurt(W_n) \qquad \text{(no target signal)}, \tag{4-24}$$

$$H_1: \quad K = kurt(W_s) \qquad \text{(target signal is present)}, \tag{4-25}$$

where K is the Kurtosis value of a specific window, kurt$\{.\}$ is the Kurtosis operator. W_n represents the window that contains only the noise while W_s refers to the first window that contains the signal peak.

By following the steps of designing a CFAR detection as mentioned in the beginning of this chapter, the next step is to find out the probability density function of H_o. However, finding the probability distribution of Kurtosis results of the FFT outputs generated by noise (H_o in our situation) is beyond the author's ability, therefore, we use an application in MATLAB, called distribution fitting function, to simulate and approach the probability plot of Kurtosis results of the noise (H_o).

In the experiments below, we first collect adequate Kurtosis results of the FFT outputs generated by noise as our samples. Then we use a group of random distribution models to fit those Kurtosis results, through empirical simulations. The empirical results are shown in Figure 4-13 for the probability plot of the Kurtosis results (H_0) approximated by different random distribution models.

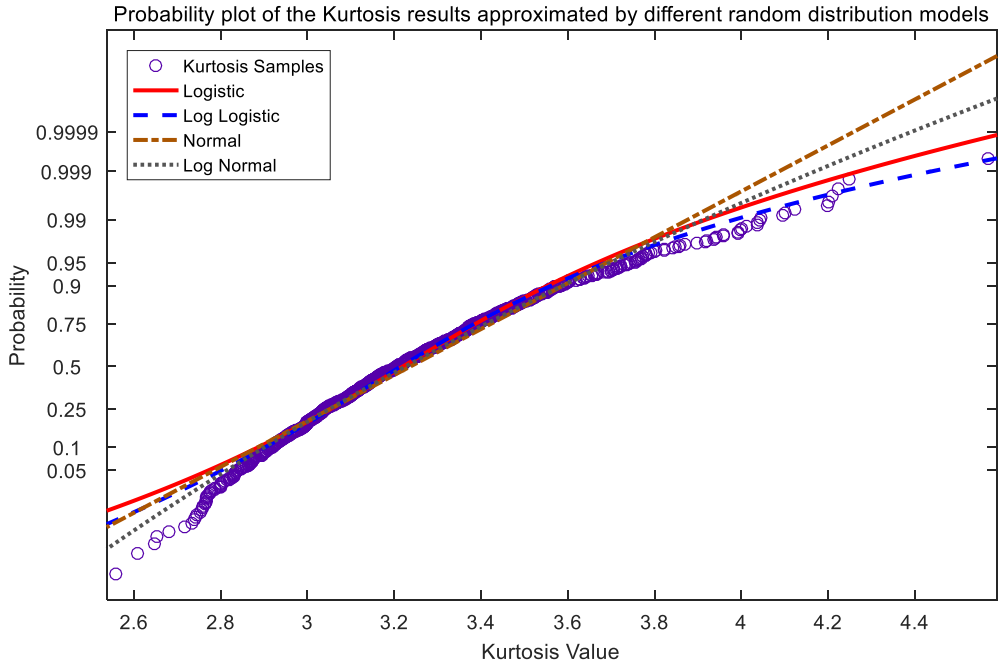

Figure 4-13. Probability plot of the Kurtosis results approximated by different random distribution models

From Figure 4-13, we can see that there are four empirical distribution models tested. Each of them has its own advantages and drawbacks. For example, the red solid line which refers to logistic distribution model approximates the kurtosis results relatively well in the right tail; however, it has much difference in the left tail. The log normal model approximates the probability curve pretty well in the left tail while it has quite errors in the right tail. In contrast, the log logistic model suits the probability curve of the samples perfectly in the right tail but no so in the left side.

Importantly, recalling from the knowledge of the CFAR detection design, we calculate the threshold of detection based on the PDF of H_0 and a given FAR (of which location is usually at the right tail of the PDF; the green area shown in Figure 4-14). Therefore, the right tail of the PDF is of a concern, as shown in Figure 4-14. Since the log logistic model is the best model to approximate the probability curve of the Kurtosis results in the right tail, in our threshold calculation module for the Kurtosis detection, the stochastic model of H_0 (Kurtosis results of the noise) can be established by the log logistic distribution, whose PDF can be expressed as [42]:

$$f(x;\alpha,\beta)=\frac{(\beta/\alpha)(x/\alpha)^{\beta-1}}{[1+(x/\alpha)]^2} \quad , \tag{4-25}$$

where α is a scale parameter and is also the median of the log logistic distribution, while β refers to the shape parameter. Once we get the expression of the PDF, we can calculate the threshold, based on the following equation:

$$FAR = P(x > K_{th}) = \int_{K_{th}}^{\infty} f(x)dx \quad , \tag{4-26}$$

where x is all of the FFT points inside the shifting window (samples), $f(.)$ is the PDF of the samples, K_{th} is the desired threshold, FAR is the given or specified false alarm rate.

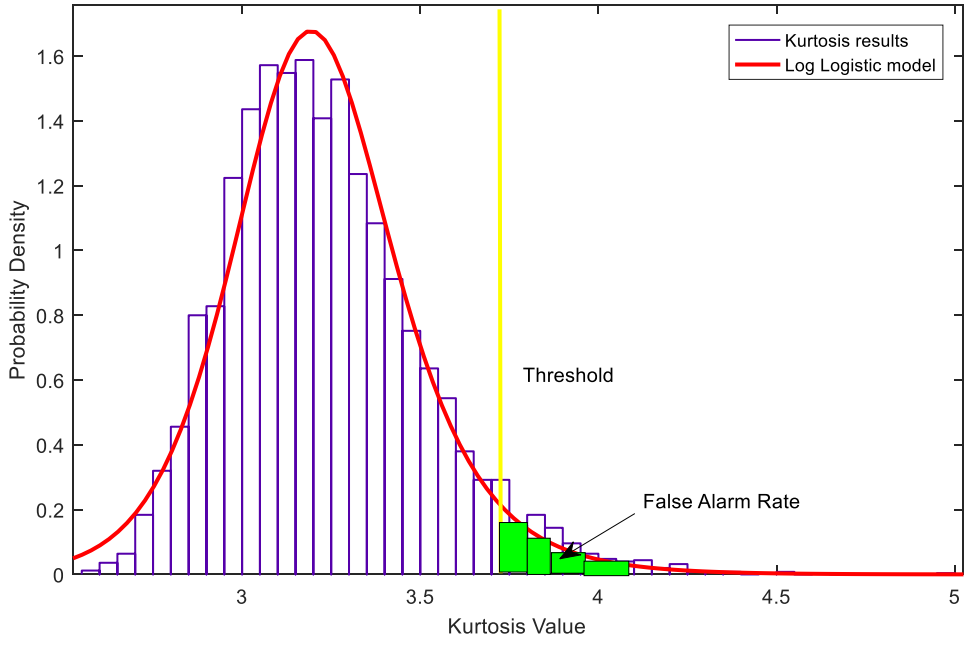

Figure 4-14. PDF of the Kurtosis results using log logistic model

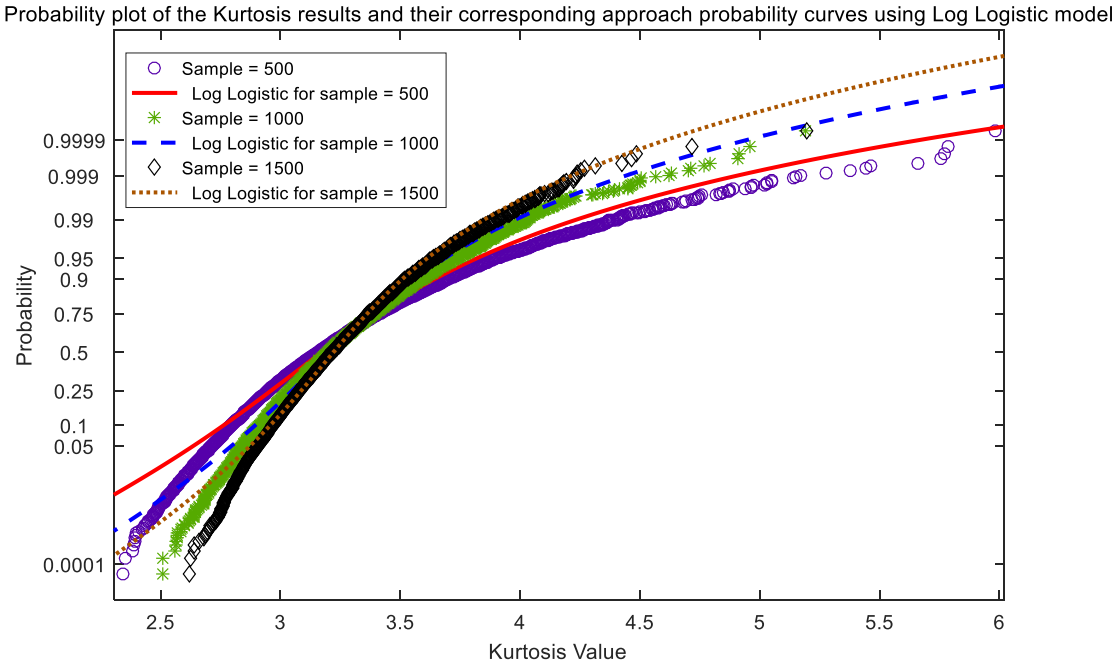

Figure 4-15. Probability plot of the Kurtosis results and their corresponding approach probability curves using Log Logistic model

Figure 4-15 shows the probability plot of H_0 with different number of samples. Here, the samples refer to all of the FFT points inside the shifting window. With the increase in number of samples, the probability curve becomes sharper and sharper, indicating that the distribution of samples become more compact. Hence, with a certain FAR, the more FFT points included in the window, the narrower the probability density function will be; it in turns makes the threshold calculated by the CFAR detection lower. Note that, for common situations, the signal-to-noise ratio, or in other words, the power of the noise will also play a crucial role in the probability distribution of the noise. However, in the Kurtosis situation, it is not true because no matter how strong the noise is, as long as the noise is still a white Gaussian noise, the Kurtosis value of the FFT results of the noise will be around 3.2 because the shape of the distribution of the noise will not change with the enhancement of its power.

Table 4-4 lists various thresholds of the CFAR Kurtosis detection with different samples inside the shifting window, when the FAR is equal to 0.0001. Clearly, with the points included in the window increase, the threshold for the CFAR detection becomes closer and closer to 3.2. The reason is because with the increase of the FFT points included in the window, the probability density function of the points becomes narrower and hence its corresponding threshold becomes closer to 3.2, which is the extreme value of the Kurtosis results of the Rayleigh random variable when the points approximate to infinity.

Table 4-4. Threshold of Kurtosis detection under different points conditions

Points	300	500	700	900	1100	1300	1500	6000	20000
K_{th}	6.59	5.74	5.32	5.04	4.86	4.74	4.64	3.8	3.58

4.3.5 Parametric Study and Performance Evaluation

In the following paragraphs, we conduct the parametric study and performance evaluation of the Kurtosis detention method. The simulations are set up with the parameters shown in Table 4-5.

Table 4-5. Parameters used in parameters study of the Kurtosis detection

Parameters	Value	Parameters	Value
f_c (GHz)	5.56	F_s (GHz)	20
T_m(ms)	2.5	E_p/N_0 (dB)	3-16 dB
B(GHz)	1.69	N_{FFT}	250000
d(m)	15	$BW_{\text{low-pass}}$ (KHz)	300
Down-sampling rate	200	$BW_{\text{high-pass}}$ (GHz)	5.0

The parameters listed here are almost the same as the parameters in Table 4-3, except for the window width W of the shifting window module and period T of the register module. These two parameters will influence the distribution of kurtosis outputs, and thus they play an important role in the performance of the Kurtosis detection. In the following part, we first study how two such parameters (the window width W and the period T) influence the distribution of kurtosis outputs respectively and then optimize parameters T and W that gives the best detection performance. Finally, we simulate the Kurtosis detection with these optimize parameters under three different channels, the AWGN channel and the multi-path channels (LOS and NLOS) .

4.3.5.1 The Parametric Study

To begin with, we need to make it clear that this parametric study is focus on effects of two parameters, T and W, only. Their optimized values can be found for the best detection probability without consideration of the channels under consideration; this is because no matter what kind of channels under consideration, whether it is LOS or NLOS, the changing tendencies of the detection probability with different T and W follow the same trend. Hence, we could study how the parameters affect the detection performance under AWGN channel and then apply the results to other complicated channel, e.g., multi-path channels. Therefore, we first focus on the AWGN channel.

A. The Effect of T

We set the window width as a constant value, 50 points, and simulate the probability of detection with different period *T*. The simulation results are shown in Fig. 4-16. As can be seen, with the increase of the period *T*, the performance of the Kurtosis method becomes better and better. In the range of about 4.5 dB to 12 dB, higher *T* tend to have a better probability of detection.

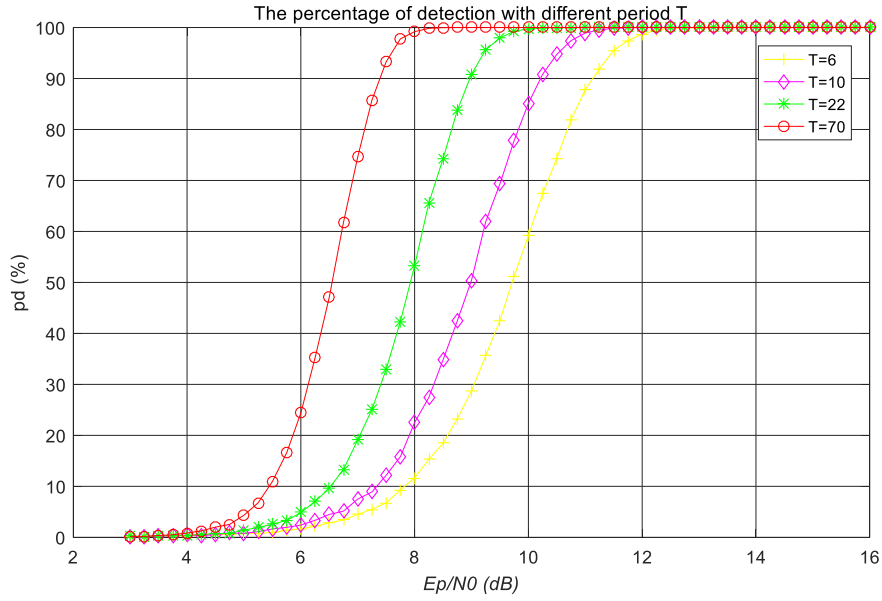

Figure 4-16. The detection probability of Kurtosis detection with different period *T*

The reason for this tendency is shown in Figure 4-17. With the increase of period *T*, the variance of the Kurtosis output of the target window decrease significantly, while the mean of the Kurtosis output of the target window stays around 4.3. As a result, based on [34], it can be shown that when the mean of the kurtosis output of the target is a constant value, the distribution of the kurtosis output that has a smaller variance will have a lower false alarm rate probability, or in other words, a higher detection probability. The explanations are shown in Figure 4-18: the blue curve represents the PDF of the target Kurtosis when *T* is 20, while the red curve refers to the PDF of the target Kurtosis when *T* is chosen as 1. It is clearly shown that with a certain threshold, the right-side area which is restricted by the threshold line; and the blue curve is larger than its counterpart under the red curve, indicating that the former has a greater detection probability than the latter. The Kurtosis detection with higher period *T* tends to have a better detection probability.

However, we are not able to increase the period *T* infinitely. On one hand, large period *T* will enhance the complexity of the detector and make itself unappealing in practice. On the other hand, we cannot assume the target will stay in the same location if the period *T* becomes too large. Because the approximate processing time for the Kurtosis detection is

calculated as $T*T_m$,, the whole processing time of the detection will become too long if T is too large, which makes it impossible to assume that the location of the target won't change in this relatively long period. Therefore, in our simulation, we let the maximum T equal 20 in order to get the optimal performance. The total computing time is TT_m=0.05s. we could safely assume that the position of the target is unchanged in this short period.

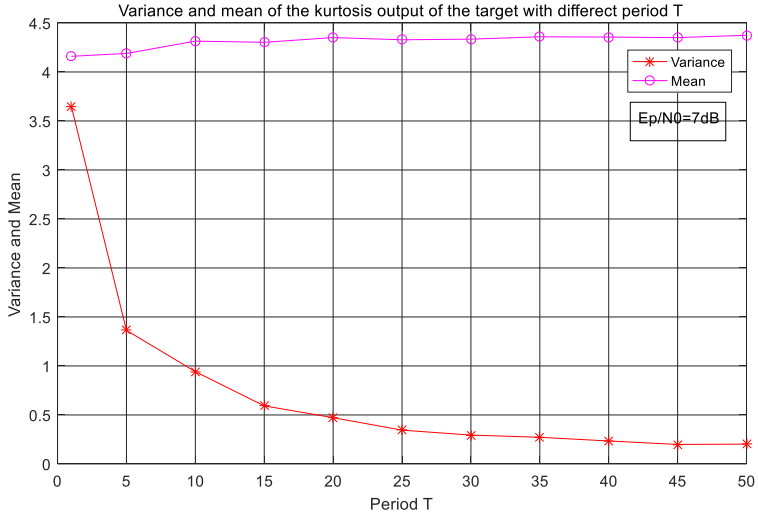

Figure 4-17. The variance and mean of the Kurtosis output of the target window with different period T

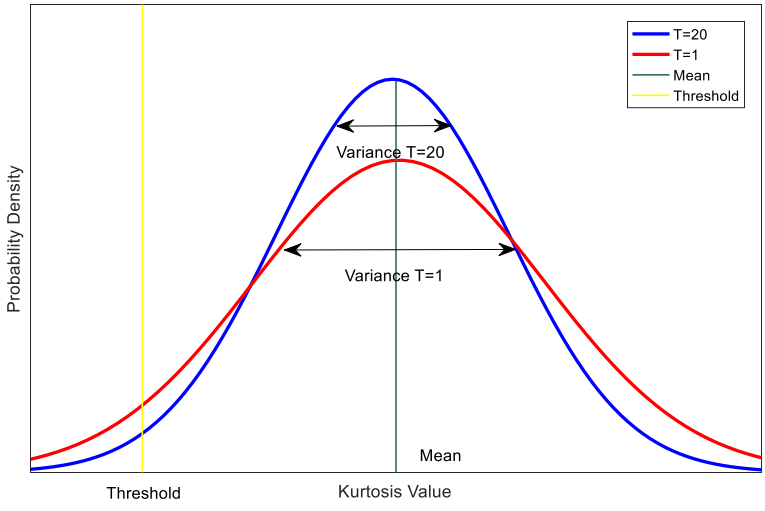

Figure 4-18. Probability density function of Kurtosis output of the target window with different T

B. Effect of W

We now set T as 20 and examine how the window width W influences the performance of Kurtosis detection. In simulation, we use 5 different window sizes (W=10, 15, 50, 75, 1000), and the simulation results are shown in Figure 4-19. We can clearly see that the Kurtosis detection with W=10 fails to work. Meanwhile, a too narrow window width (W=15) or too wide window width (W=1000) also have poorer probability of detection than moderate window width (W=*50* or *75*), for E_p/N_0 ranging from 6 dB to 11 dB. The reasons are related to the variance and mean of the kurtosis output of the target. First, based on the discussion before, the increase of the total points ($T \cdot W$) that we use to calculate the kurtosis output will decrease the variance of the kurtosis output. Thus, since the period T is unchanged, the variance of the kurtosis output will become smaller with the increase of the window width W. However, unlike with the situation in Kurtosis detection with different period T where the detector with a smaller variance tends to have better performance, the situation with different W is more complicated, because not only is the variance related to the parameter W, but also the mean value of the kurtosis output also changed with W.

As shown in Figure 4-20, the mean value of the Kurtosis output of the target window follows a parabolic form of change. For different E_p/N_o, the optimal W which could provide us with the largest mean is slightly different. However, the larger mean value doesn't mean a higher probability of detection because the detection probability is also influenced by the variance; as shown in figure 4-21, with the increase of window width W, the variance of the Kurtosis outputs decreases steadily. Therefore, in order to figure out how the parameter W influences the detection probability, we have to analyze the problem in terms of both the variance and the mean.

From Figure 4-20, it is true that the window width W of 15 has a larger mean than the window width W of 50; but the latter has a much smaller variance than the former, as shown in Figure 4-21. When we display it in a PDF graphic, it can be shown as Figure 4-22. The blue curve shows the probability density function of the Kurtosis outputs when we set the window width W as 50, while the red curve represents the PDF of the Kurtosis outputs when the window width W is equal to 15. From the figure, we can clearly see that although the blue curve has a smaller mean value, its variance is also smaller than the red curve. Therefore, as a correlative result, in the right-side area which is restricted by the threshold line, the blue curve is larger than its counterpart of the red curve. Hence, recalling its mathematical meaning, we can say that the probability of detection for Kurtosis detector whose W is 50 is higher than the one with W equaling to 15, when E_p/N_0 ranges from 6 dB to 11 dB. In contrast, although the variance of Kurtosis detector with W of 1000 is much relatively smaller than the detector with W of 50, the performance of the latter is far better than the former (shown in Figure 4-19), simply because the Kurtosis detector with W of 50 has a dramatically greater mean value than the Kurtosis detector with W of 1000. To make it clear, we draw the PDF of these situations in Figure 4-23. The blue curve refers to the PDF when the window width is 50, which has a relatively larger variance as well as a greater mean value. Meanwhile, the red curve shows the PDF when the window width of

the detector is chosen as 1000, which has a slightly smaller variance but a much significantly smaller mean value than the detector with W of 50. Obviously, the right-side area under the blue curve is larger than its counterpart under the red curve, indicating that a detector with W =50 does have a higher detection probability that the one with W of 1000. Based on the above analysis, we conclude that a moderate window width can assure a better performance of Kurtosis detection. Thus, in the following simulation, we choose the widow width as 50 to maintain a relatively high detection probability.

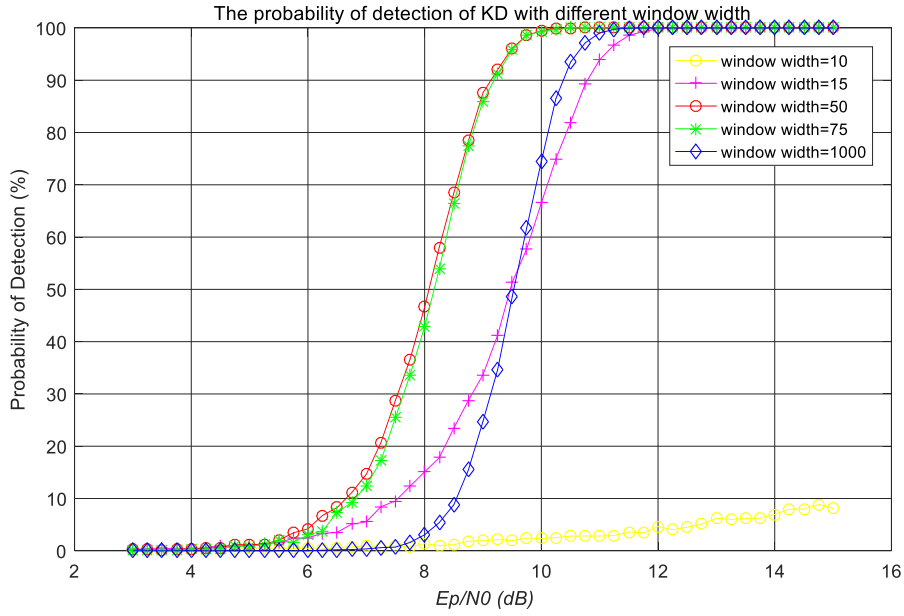

Figure 4-19. The detection probability of Kurtosis detection with different window width

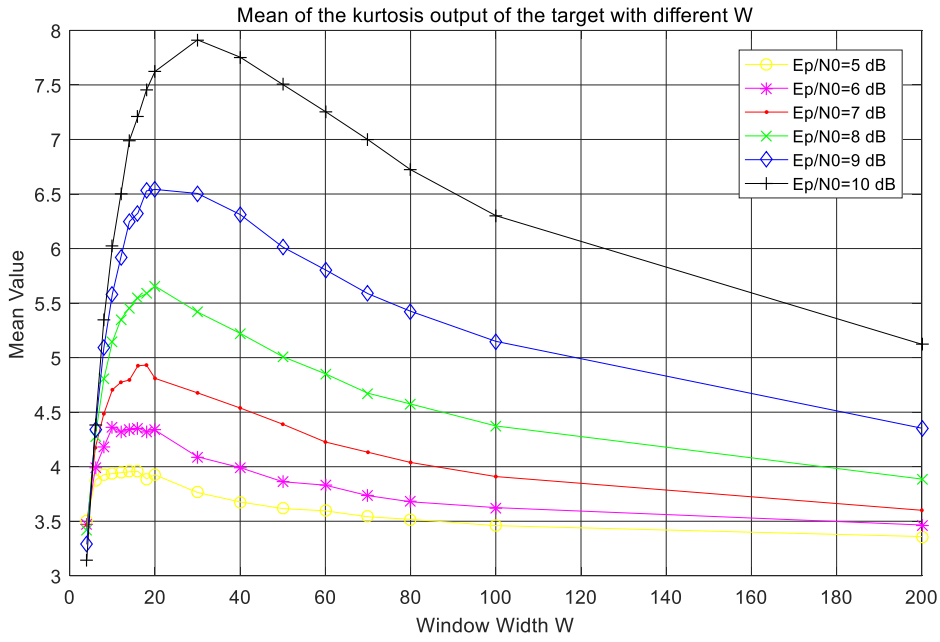

Figure 4-20. Mean of the Kurtosis output of the target window with different window width

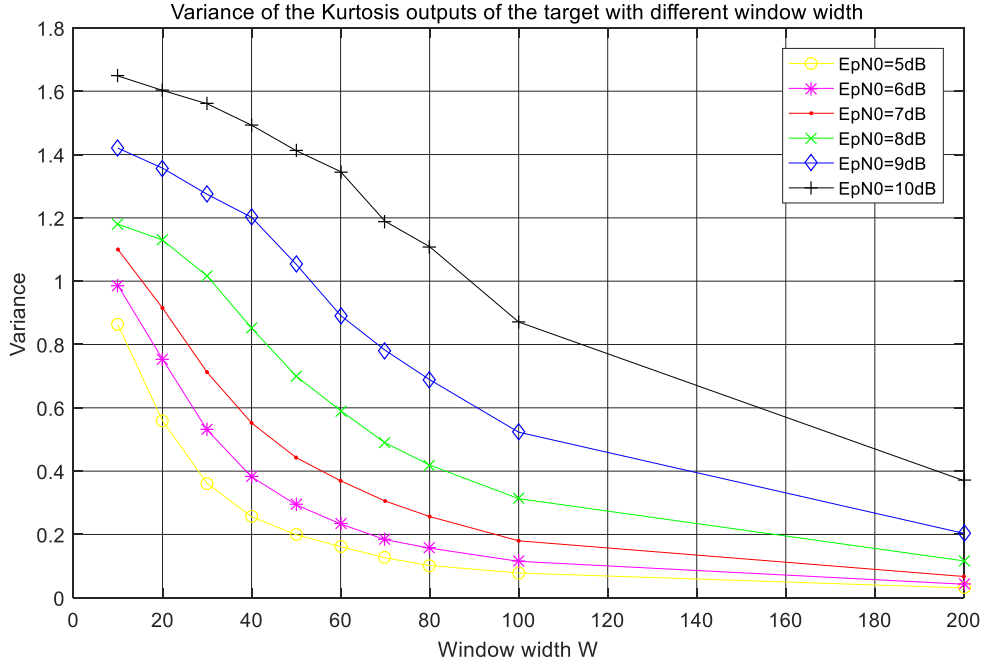

Figure 4-21. Variance of the Kurtosis output of the target window with different window width

Note that since we use 50 points as our window width, it means that we assume that in the beginning 50 FFT bins, there is no signal impulse in this region. Using the knowledge of FMCW radar system, the minimum feasible distance $d_{\min}$ of the target can be calculated as:

$$d_{\min} = \frac{W \cdot \Delta f_{\min} \cdot T_m \cdot c}{2B} \quad , \tag{4-27}$$

where $\Delta f_{\min}$ is the size of one bin of the FFT, T_m is the duration of FMCW signal, c is the speed of light, B is the maximum shift bandwidth of the FMCW signal, W is the window width we use in the Kurtosis detection. In our situation, since we choose W as 50 points, $d_{\min}$ is equal to 4.43m as computed with Equation (4-27).

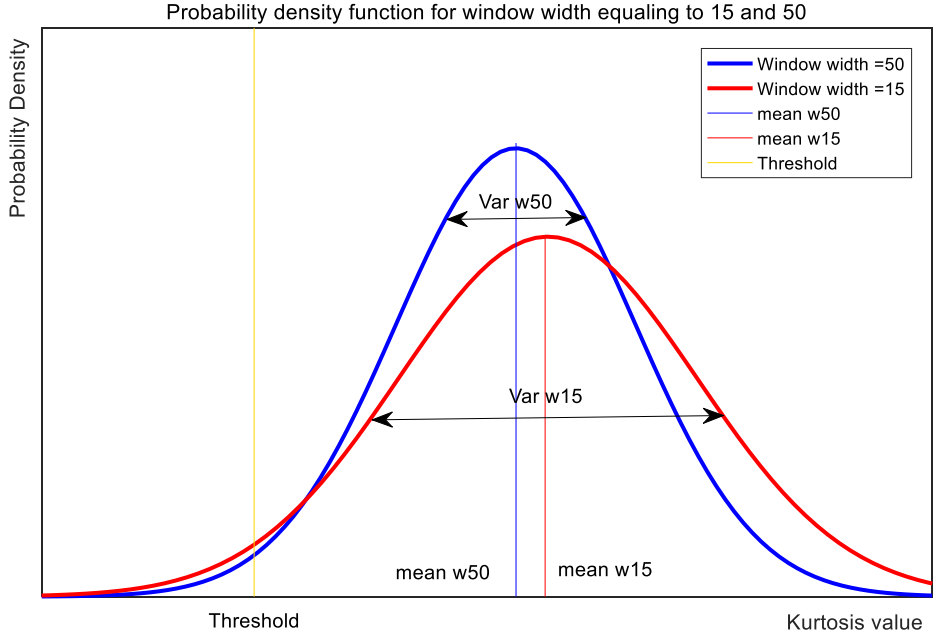

Figure 4-22. Probability density function for window width equal to 15 and 50

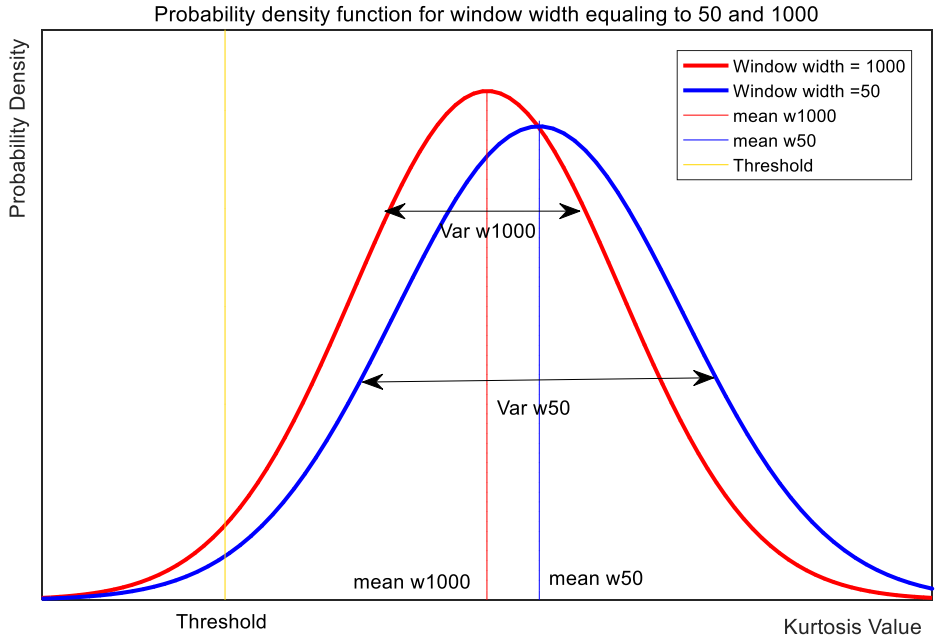

Figure 4-23. Probability density function for window width equal to 50 and 1000

4.3.5.2 Performance Evaluation

Previously, we have done the parametric study and select a pair of appropriate parameters for proposed Kurtosis detector (T=20, W=50). In this section we will simulate the Kurtosis detector under different channels. The parameters used are shown in Table 4-3 and the simulation results are presented in Figure 4-24 and Figure 4-25.

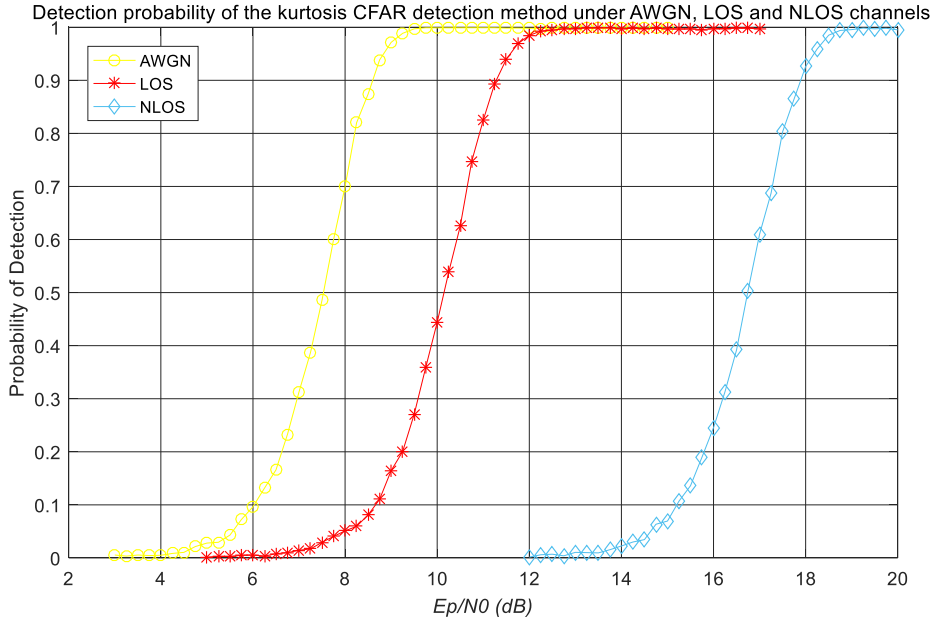

Figure 4-24. Detection probability of the kurtosis CFAR detection method under AWGN, LOS and NLOS channels

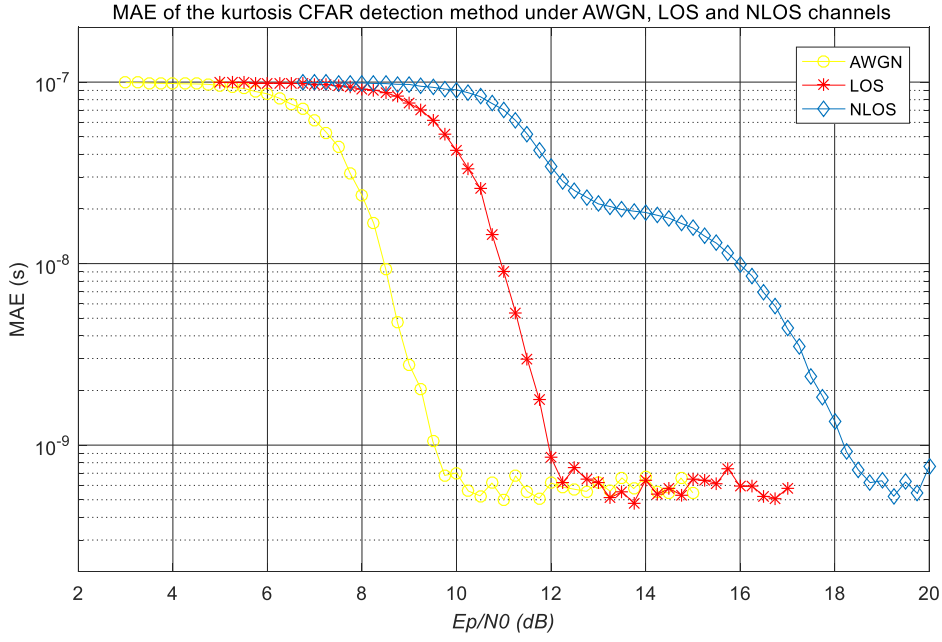

Figure 4-25. MAE of the kurtosis CFAR detection method under AWGN, LOS and NLOS channels

From Figure 4-24, it is clear the three curves representing the performances under three channels follow the same trend, indicating that the detection probability becomes higher with the increase of E_p/N_0 (signal to noise ratio). Specifically,, the AWGN curve for Kurtosis detection starts to climb first and reaches its maximum when E_p/N_0 is just over 9dB. The LOS curve hits its maximum value when E_p/N_0 is about 12dB, while the NLOS curve is the last one to achieve its best performance until the E_p/N_0 has increased to approximate 18.5dB. Such results are expected: the AWGN channel is the ideal channel where all of the energy was concentrated on the target impulse, while the NLOS channel is the worst channel in which most of the energy is occupied by the multi-path reflections. All three curves share similar maximum detection probability around 99.8%, which is distinctly better than the best detection probability for the conventional detection (98.2%). This is because for the conventional CFAR detection, to find the target impulse, it has to compare all of the FFT bins before the target FFT bin with the threshold. As a result, the total processing time is relatively large. For the proposed Kurtosis CFAR detection, its total processing time is much smaller than the conventional CFAR detection because of the characteristic of the bisection method. Therefore, even if we use the same constant false alarm rate, the maximum probability of detection for the Kurtosis detection is significantly better than that of the conventional detection.

Figure 4-25 shows the same conclusions as Figure 4-24: with the increase of signal-to-noise ratio, the MAE of the TOF becomes smaller. Also, in a moderate signal-to-noise ratio of 6dB to about 19dB, the yellow curve (AWGN) tends to have the smallest MAE while the blue figure (NLOS) always has the largest MAE, illustrating that the AWGN channel has the best performance while the performance of detection under NLOS channel is always the worst. After the signal-to-noise ratio has increased to 19 dB, all of these figures arrive at the minimum MAE around $0.5\text{x}10^{-9}$s, which is lower than the minimum MAE for the conventional detection. This is agreeable with the fact that the maximum detection probability for Kurtosis detection is greater than the conventional detection. Similarly to that in the conventional detection, there is also a 'plateau' in the MAE curve under NLOS channel. The reason for such phenomenon has been explained in section 4.2.2.

4.4 The Proposed Skewness Detection

In the previous section, a new Kurtosis detection has been proposed, studied and evaluated. Compared with the conventional CFAR detection, Kurtosis detection, which is based on the statistic characteristics of the input data, is more accurate and has higher reliability in a moderate SNR region. In this section, we study and simulate another statistic detection which is based on the third standardized moment, known as Skewness. The structure and working process of the Skewness detection is almost similar to the previous Kurtosis

detection, except that right now, we use Skewness value to identify the target impulse rather than using Kurtosis value.

The organization of this section is as follows. First, we define Skewness and how it can be used to enhance the performance of detection. Then, the structure and implementation of the Skewness detection is shown. Next, we calculate the threshold of the Skewness detection based on a given false alarm rate. Finally, we evaluate the performance of the Skewness detector under different channels, including AWGN, LOS and NLOS.

4.4.1 The Third Standardized Moment, i.e., Skewness

The Skewness, which is also called the third standardized moment, is a measure of the asymmetry of the probability distribution of a real-valued random variable about its mean [43]. Its definition is:

$$Skew(x) = \frac{E[(x-\mu)^3]}{(E[(x-\mu)^2])^{3/2}} \tag{4-28}$$

where E{.} represents the expectation operator and u is the mean of the variable x.

For some limited samples whose length is N_{sa}, its Skewness value can be estimated as:

$$Skew(x) \approx \frac{\frac{1}{N_{sa}}\sum_{i=1}^{N_{sa}}(x_i-\bar{x})^3}{\{\frac{1}{N_{sa}}\sum_{i=1}^{N_{sa}}(x_i-\bar{x})^2\}^{3/2}} \quad , \tag{4-29}$$

where N_{sa} is the total sample number of the variable x, $\bar{x}$ is the mean of the samples.

According to [44], there are several types of the sample histograms with the Skewness technique, as shown in Figure 4-26. The three columns of the figures in Fig. 4-26 are the most usual and simple examples for a probability distribution. For those in the left column of Fig. 4-26, they are called ‘Skewed Left’: the mass of the distribution is concentrated on the right of the figures and the left tails are longer than the right tails; its corresponding Skewness value is always negative. For those in the right column of Fig. 4-26, they are called ‘Skewed Right’: the mass of the distribution is concentrated on the left of the figures and the right tails are longer than the left ones; its corresponding Skewness value is always positive (e.g., Rayleigh distribution conforms to a typical ‘Skewed Right’ model). For those in the middle column of Fig. 4-26, they are called ‘Symmetric’; their Skewness values tend to be zero.

As mentioned earlier, during the digital processing, the FFT bins caused by the noise follow a Rayleigh distribution. Hence, the shifting window in the frequency domain, which contains only the FFT bins caused by the noise, is a typical 'Skewed Right' model, and has its own corresponding Skewness value. Through the empirical simulations, we find that the skewness value of the noise window is not related to the power of the noise but is influenced by the number of the samples inside the noise window. When the number of the samples inside the noise window is large enough, the Skewness value converges to 0.62. However, when the window contains both the noise and the target impulse, then the model is no longer a 'Skewed Right' distribution but a 'Right Tail Extremes' distribution. In this situation, although the Skewness value is still positive, it becomes much larger than the one with only noise inside the window. Based on this characteristic, we can design a Skewness detection to locate the target impulse, imitating the structure and process of the Kurtosis detection.

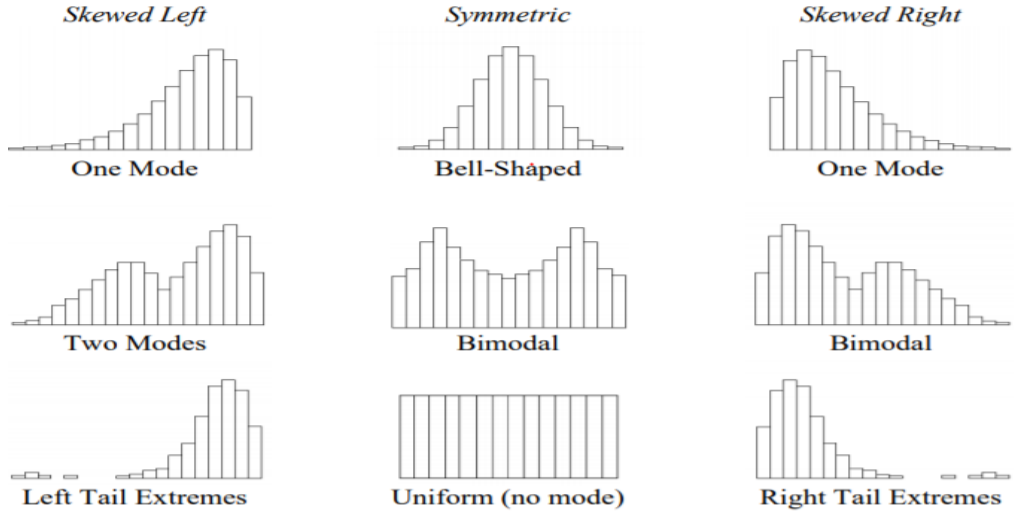

Figure 4-26. Illustrative histograms with Skewness statistic [45]

4.4.2 The Structure and Working Process of Skewness Detection

The structure of the proposed Skewness detector has been shown in Figure 4-27. Compared with the Kurtosis detection, the only difference is that in Skewness detection, we use the Skewness estimation module to replace the original one. The other parts are all the same with the Kurtosis detection. In Skewness detection, we also use a register module to collect enough samples and use a shifting window module to detect the position of the target impulse. The bisection method can also be implemented in Skewness detection. Although similar to Kurtosis detection, the threshold calculation for the Skewness detection is completely different from Kurtosis detection because the probability distribution of the statistic results (Kurtosis results or Skewness results) of the FFT bin caused by the noise

are totally different; it in turn makes the value of the threshold different even though both Kurtosis and Skewness detection use the same false alarm rate. This will be discussed in the next section.

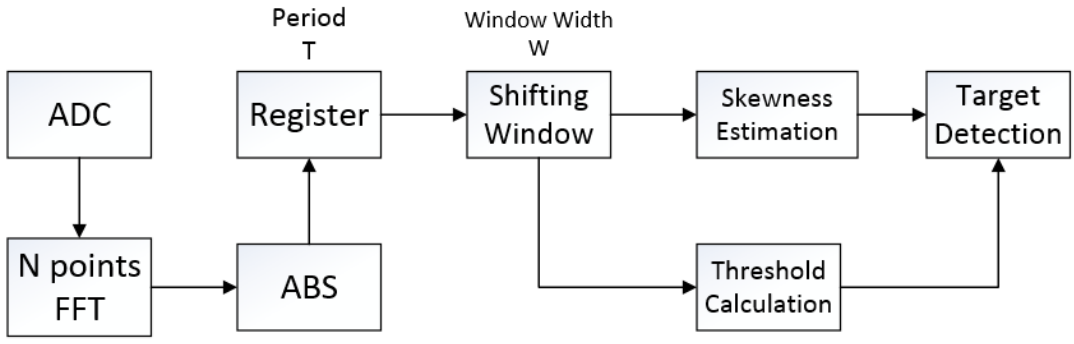

Figure 4-27. The structure of the proposed skewness CFAR detection

4.4.3 Calculating the Threshold of Skewness Detection

Similarly to the threshold calculation module for Kurtosis detection, we use the distribution fitting function in the MATLAB software to simulate and approach the probability plot of Skewness results of the noise, which is one of the hypothesis in the detection processing (H_0). Please refer to sections 4.1 and 4.2 for more details.

By doing the experiments similar to those for the Kurtosis detection, we first collect adequate Skewness results of the FFT outputs generated by noise as our samples. Then we use a group of random distribution models to fit the Skewness results to the empirical simulation results. The empirical results are shown in Figure 4-28 for the probability plot of the Skewness results (H_0) approximated by different random distribution models.

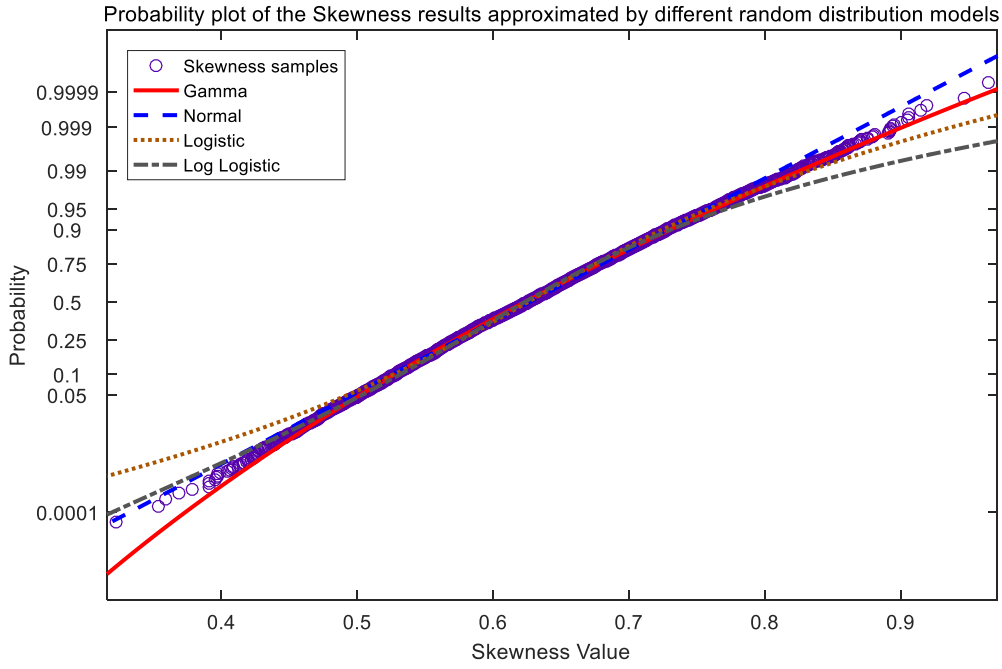

Figure 4-28. Probability plot of the Skewness results approximated by different random distribution models

From Figure 4-28, four empirical distribution models tested. Each has its own advantages and drawbacks. For example, the red line which refers to the gamma model, approximates the Skewness results relatively well in the right tail; however, there is a relatively wide difference in the left tail. Both normal and log logistic models approximate the probability curve more accurately in the left tail than the gamma model and logistic model, while their matches in the right tail are quite unsatisfactory. Recalling the CFAR detection design, we calculate the threshold of detection based on the PDF of H_0 and a given FAR, of which the area is usually at the right tail of the PDF (the green area shown in Figure 4-29). Therefore, the most concern is the right tail of the PDF, as shown in Figure 4-29. Since the gamma model is the best model to approximate the probability curve of the Skewness results in the right tail, in our threshold calculation module for the Skewness detection, the stochastic model of H_0 (Skewness results of the noise) is established with the gamma distribution; the corresponding PDF can be expressed as [46]:

$$f(x,\alpha,\beta)=\frac{\beta^{\alpha}x^{\alpha-1}e^{-\beta x}}{\Gamma(\alpha)} \quad , \tag{4-30}$$

where α is a shape parameter and β is an inverse scale parameter which is also called a rate parameter. The denominator is a complete gamma function. Once we get the expression of the PDF, we can calculate the threshold, based on the following equation:

$$FAR = P(x > S_{th}) = \int_{S_{th}}^{\infty} f(x)dx \quad , \tag{4-31}$$

where x is all of the FFT points inside the shifting window (samples), $f(.)$ is the PDF of the samples, S_{th} is the desired threshold and FAR is the given or specified false alarm rate.

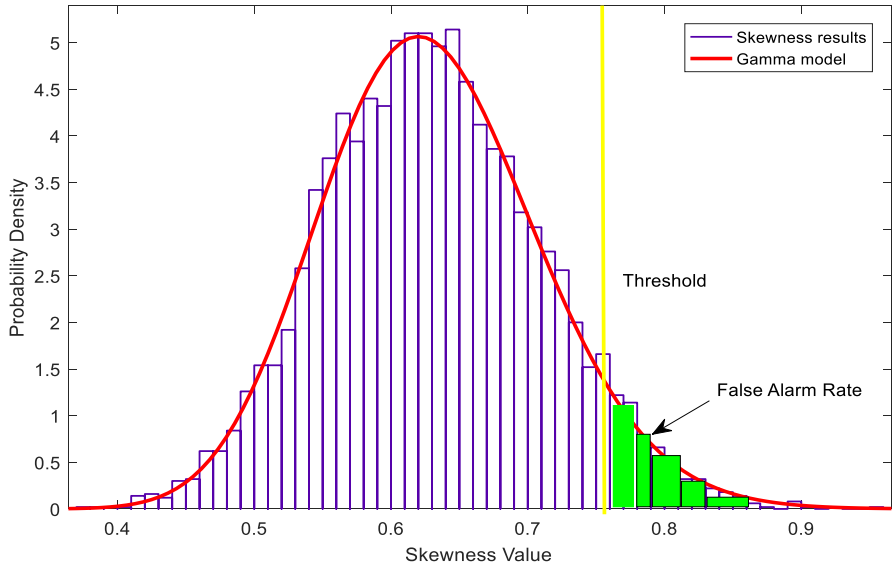

Figure 4-29. PDF of the Skewness results using gamma model

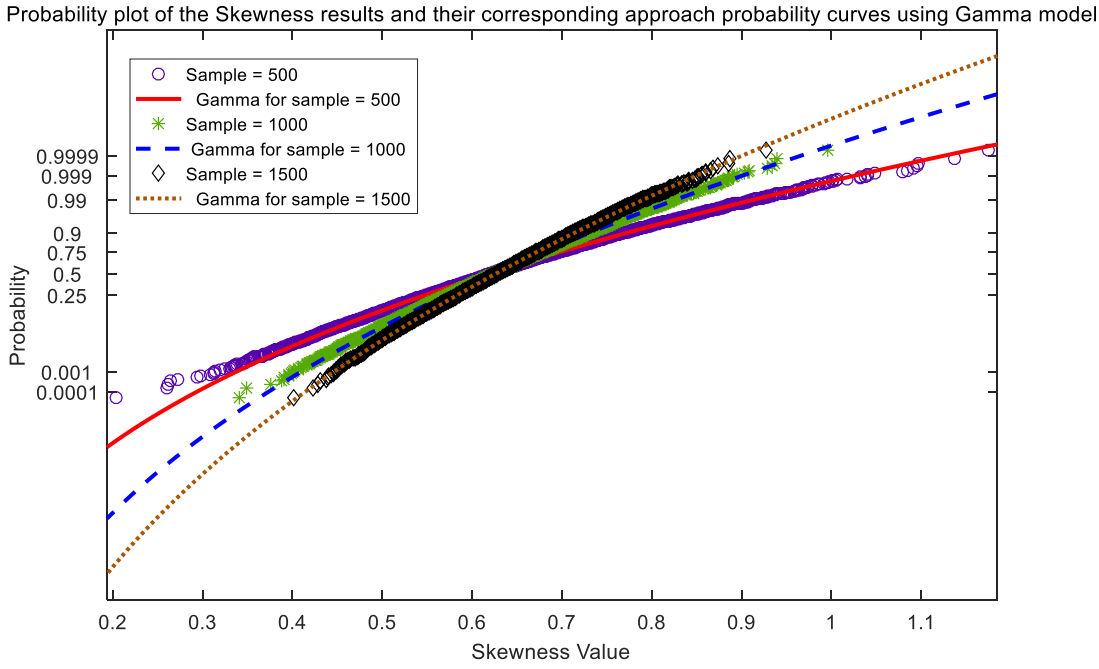

Figure 4-30. Probability plot of the Skewness results and their corresponding approach probability curves using Gamma model

Figure 4-30 shows the probability plot of H_0 with different numbers of samples. Here, the samples refer to all the FFT points inside the shifting window. With the increase of number of samples, the probability curve becomes sharper, indicating that the distribution of samples become more compact. Hence, with a certain FAR, the more FFT points included in the window, the narrower the probability density function will be; it in turns makes the threshold calculated by the CFAR detection lower. Notice that, in common situations, the signal-to-noise ratio, or in other words, the power of the noise, will also play an important role in the probability distribution of the noise. However, in the Skewness situation, it is not true because no matter how strong the noise is, if it is still a white Gaussian noise, the Skewness value of the FFT results of the noise will be around 0.65 because the shape of the distribution of the noise won't change with its power.

Table 4-6 lists various thresholds of the CFAR Skewness detection with different samples inside the shifting window, when the *FAR* is equal to 0.0001. Clearly, with the number of the points in the window increases, the threshold for the CFAR detection becomes closer to 0.65. The reason is because with the increase of the FFT points included in the window, the probability density function of the points becomes narrower and hence its corresponding threshold becomes closer to 0.65, which is the extreme value of the Skewness results of Rayleigh random variable when the samples approximate to infinity.

Table 4-6. Threshold of Skewness detection under different points conditions

Points	300	500	700	900	1100	1300	1500	6000	20000
Th	1.32	1.21	1.04	0.99	0.95	0.92	0.9	0.76	0.67

4.4.4 Performance Evaluation

In section 4.3, we perform the parametric study and obtain a pair of appropriate parameters for proposed Kurtosis detector (T=20, W=50). In this section, we will simulate the performance of the Skewness detector under different channels, using the same parameters we set for the Kurtosis detection. The specific parameters are listed in Table 4-7 and the results are shown in Figures 4-31 and 4-32.

Table 4-7. Simulation parameters used for the Skewness CFAR detection

Parameters	Value	Parameters	Value
f_c (GHz)	5.56	F_s (GHz)	20.0
T_m(ms)	2.5	E_p/N_0 (dB)	15
B(GHz)	1.69	NFFT	2.5*e5
d(m)	15.0	$BW_{\text{low-pass}}$ (KHz)	300
Down-sampling rate	200	$BW_{\text{high-pass}}$ (GHz)	5
T	20	Window Width W	50

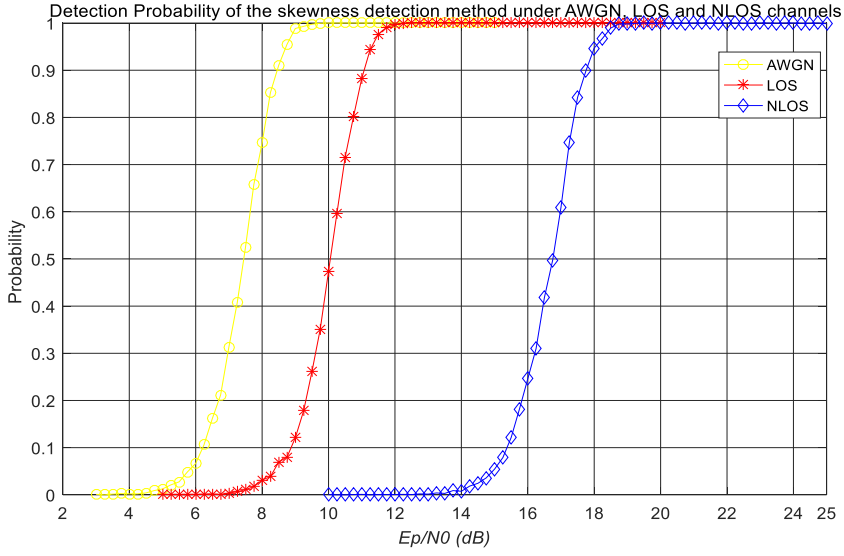

Figure 4-31. Detection probability of the skewness CFAR detection method under AWGN, LOS and NLOS channels

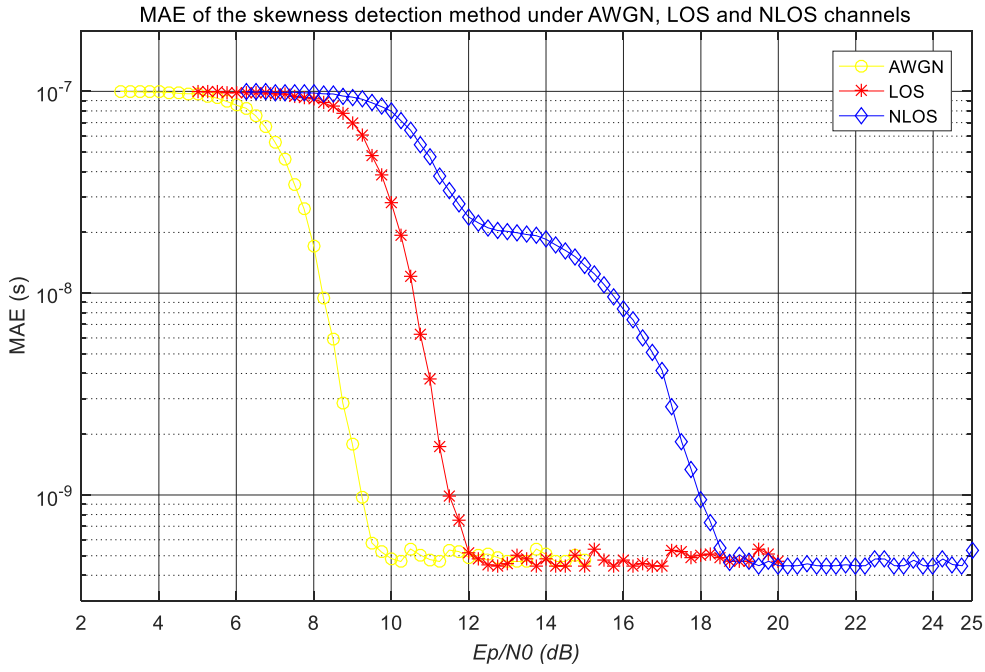

Figure 4-32. MAE of the skewness detection method under AWGN, LOS and NLOS channels

The simulation results of detection probability for Skewness detection are similar to those for Kurtosis detection. At about 9 dB, the detection under AWGN channel reaches its maximum value, followed by the LOS curve which arrives at its peak at 12dB. The last one that hits its maximum is the NLOS curve, when the signal-tio-noise ratio increases to slightly lower than 19dB.

The results of MAE are agreeable with the results of detection probability: with the improvement of E_p/N_0, the MAE will decrease gradually and reaches its valley; the valley is around $5\text{x}10^{-9}$s and the corresponding signal-to-noise ratios are 9.5 dB, 12.0dB and 19.0 dB under AWGN, LOS and NLOS channel, respectively. Besides, when the signal-to-noise ratio is smaller than 5 dB, all of the MAE with these three channels stay constant at 10^{-7}s. This is because at this region, the signal is too weak to be detected successfully. There is not even one FFT bin of which the value can exceed the threshold we set. In this situation, the detection methods will set the estimated TOF as 0s. The MAE can be calculated as:

$$MAE = \tau - \hat{\tau} = \frac{2d}{c} = 10^{-7} \quad , \tag{4-32}$$

where d is the distance between the target and the antennas, c is the speed of light. Additionally, like the other two detection we introduced, there is also a 'plateau' in the

NLOS curve between 12 dB to 14 dB for the Skewness detection. The reasons for this have been explained in section 4.2.2.

4.5 Performance Comparison and Discussion

In the previous three sections, we have studied three different detection methods by simulating them under three different channels respectively. In this section, we will compare the performances of these detection methods under different channels and draw conclusions. Since the detection probability and MAE are only two different ways to evaluate the performance of the detection and they have presented the same information on the performances of each individual detection, respectively. In this section, we will focus only on the comparison of the MAE results. Another reason for choosing MAE rather than detection probability is that the former uses non-linear expression and hence can show more insights about our results. The simulation results are shown in Figs. 4-33, 4-34 and 4-35.

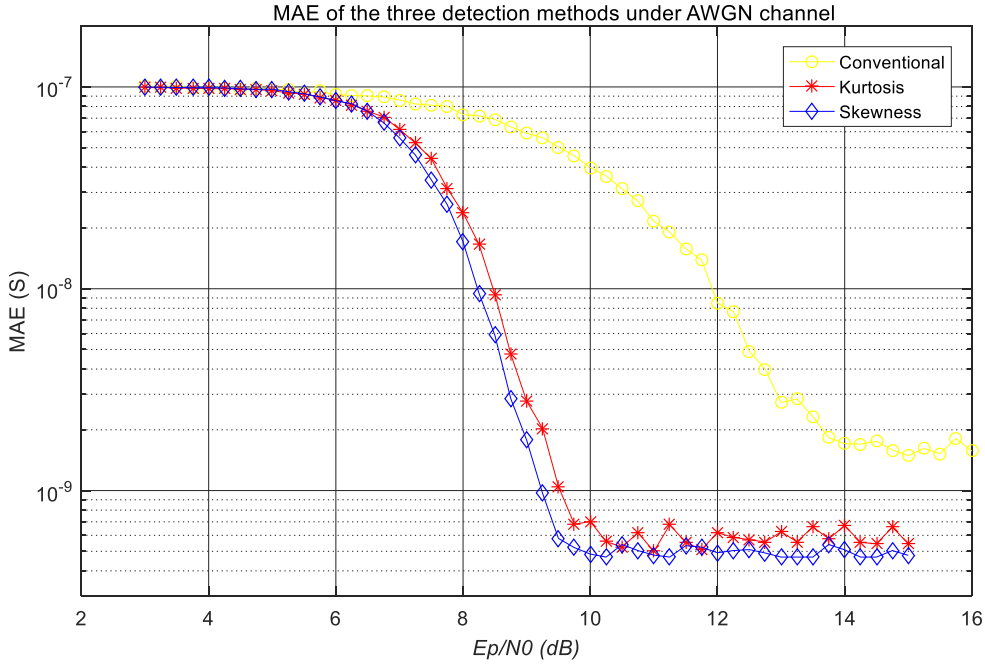

Figure 4-33. MAE of the three detection methods under AWGN channel

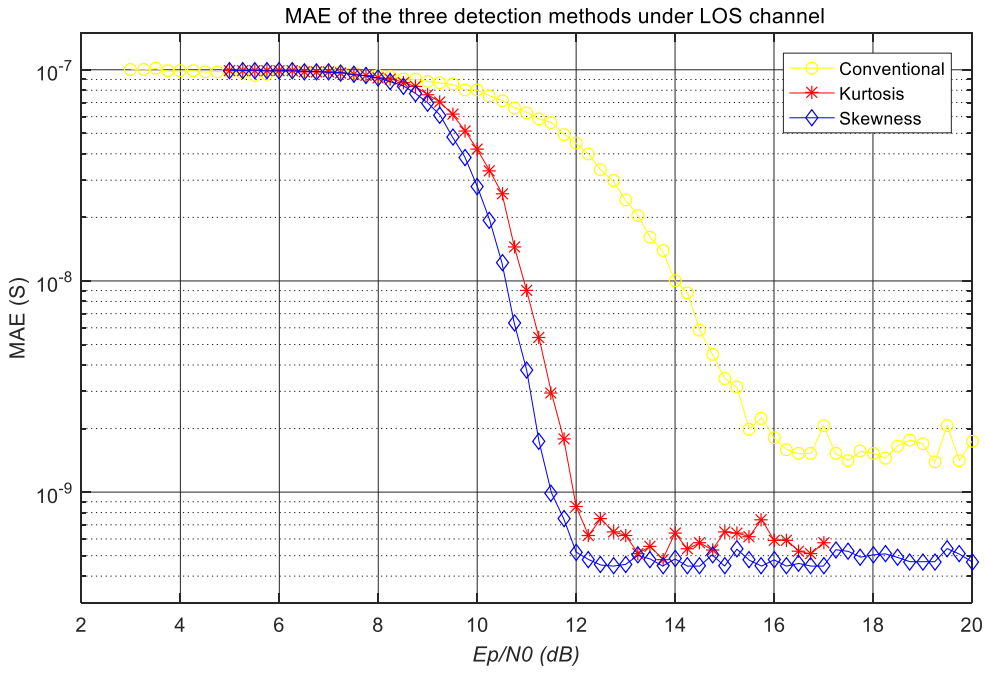

Figure 4-34. MAE of the three detection methods under LOS channel

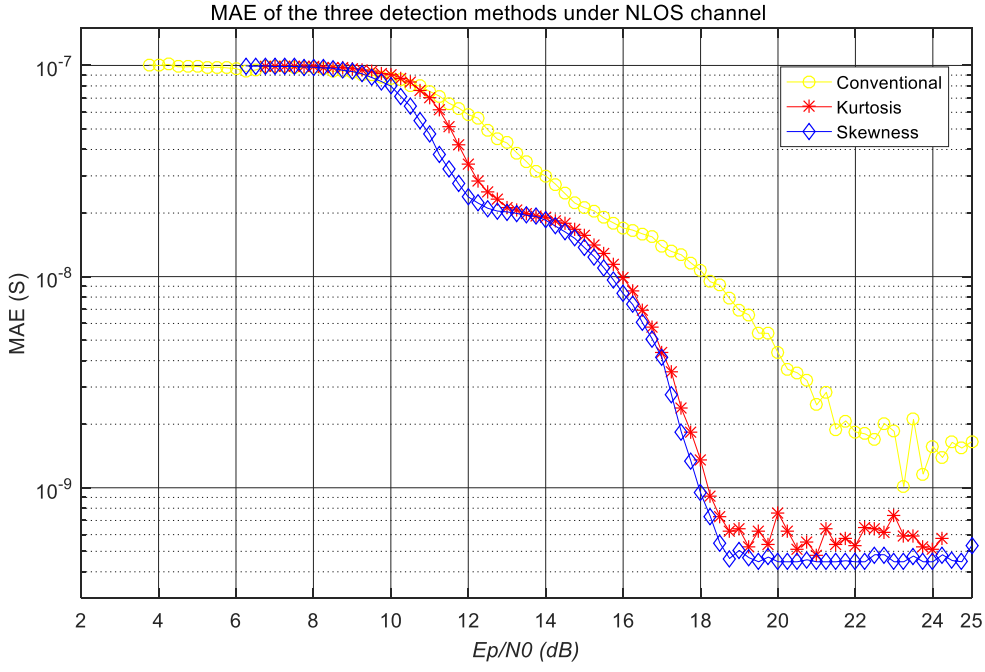

Figure 4-35. MAE of the three detection methods under NLOS channel

From the above figures, it is quite evident that both the proposed Kurtosis and Skewness detection have much better detection performance than the conventional detection under

these three channels, while the Skewness detection outperforms the Kurtosis detection a little bit.

In AWGN channel, MAE curves for both of the Skewness and Kurtosis detection start to fall significantly at about the signal-to-noise ratio of 6dB, and hit a valley almost at the same at the signal-to-noise ratio of 9.75dB. During this falling process, it is important to mention that the slope of the Skewness detection is mildly sharper than the Kurtosis detection. However, it is not until the signal-to-noise ratio of 8 dB that the MAE curve for the conventional detection begins to decrease and arrives at its minimum value at 14dB. Except for the different falling speed, the minimum value of the MAE that a specific detection can obtain is also different for the three detection methods. The conventional detection can only maintain a minimum MAE value at about $2x10^{-9}$s when the signal-to-noise ratio is large enough. Whereas, the Kurtosis detection can obtain a minimum MAE at around $6x10^{-10}$s and Skewness detection slightly outperforms the Kurtosis detection with the lowest minimum MAE around $5x10^{-10}$s.

Similar trends are found in Figure 4-34 for LOS channel. The MAE curve for the Skewness detection and Kurtosis detection begin to decrease at the signal-to-noise ratio of 8dB, where the former has a sharper slope. Both of them get to their minimum values of $6x10^{-10}$s and $5x10^{-10}$s, respectively when the signal-to-noise ratio is just over 12dB. In comparison, the performance of the conventional detection is not as good as these two statistic-based detection methods. Its MAE starts to fall apparently at the signal-to-noise ratio of 10 dB and reaches its lowest points at the signal-to-noise ratio of 16dB. Besides, its obtainable minimum MAE is only $1.5x10^{-9}$s.

Except for the common trend that with the increase of the signal-to-noise ratio and the MAE will decrease gradually with all three detection methods, there is a ‘plateau’ in the middle of the curves with all three detection methods. For Skewness and Kurtosis detection, the ‘plateau’ is within the region of 12.5 dB to 14 dB of the signal-to-noise ratio, while for conventional detection, there is also a similar ‘plateau’ between 15 dB to 17 dB under the NLOS channel. This can be explained as follows. Under the NLOS channel, the strongest FFT bin is usually not the target impulse as shown in Figure 4-36. When the signal-to-noise ratio is quite low, e.g., smaller than 8 dB, all the reflected signals are inundated in noise and hence the MAE stays at 10^{-7}s. As the signal-to-noise ratio becomes stronger than 8dB, the detection starts to detect the signal impulse successfully. However, at this point, the most possible signal impulse for the system to detect is the strongest reflecting signal. With the continuous improvement of signal-to-noise ratio, it becomes possible that the second strongest reflected signal is detected. There is a region of the signal-to-noise ratio (e.g., 12.5 to 14 dB with Skewness detection), the detector keeps considering the second strongest peak as the target impulse. As a result, the MAE keeps constant in this region. With further increase of the signal-to-noise ratio, the detector begins to detect the target impulse successfully. When the signal-to-noise ratio increases to a strong enough value

(e.g., 18.5 dB with Skewness detection), the MAE arrives at its minimum value which is slightly higher than 4.5×10^{-10}s.

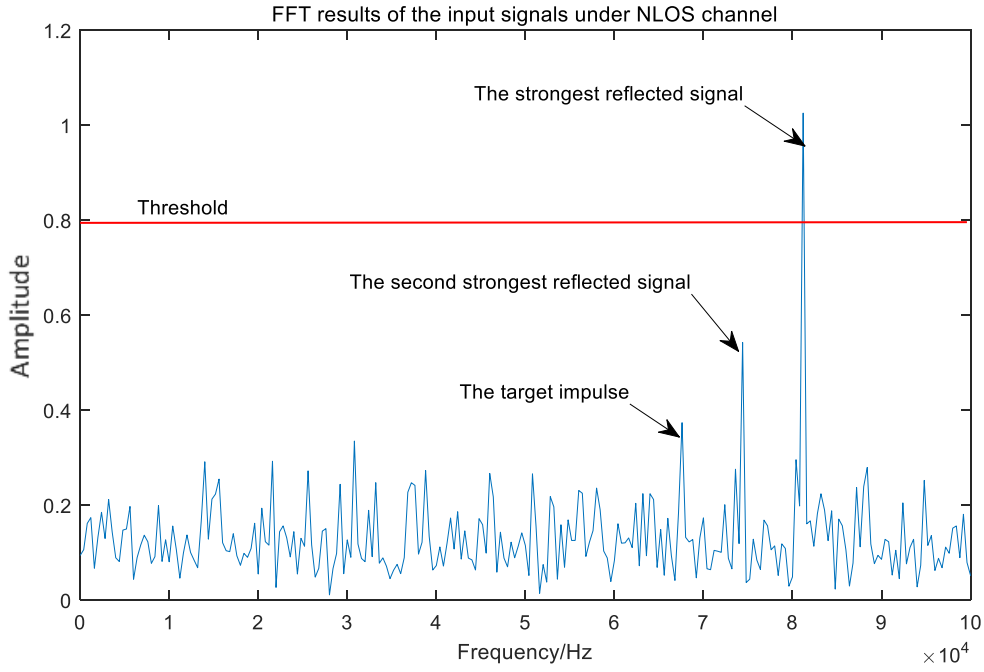

Figure 4-36. FFT results of the input signals under NLOS channel

In a word, based on the above three figures, we conclude that both of Skewness and Kurtosis detections outperform the conventional detection to a great extent after the signal-to-noise ratio exceeds a particular value (such a value dependent on the types of channels and detection methods). Our simulations show that Skewness detection is slightly better than the Kurtosis detection in both the MAE falling slope as well as the minimum MAE that a detection method can achieved.

CHAPTER 5 CONCLUSION AND FUTURE WORK

5.1 Conclusion

This dissertation presents the principle and implementation of an indoor radio tracking system using FMCW radar signal. Compared with the conventional localization system, such as RF localization (which uses WiFi and other communication systems to track the target) and other imaging systems, e.g, Kinect, the indoor FMCW radio tracking system has three advantages. First, it does not require targets to carry any wireless devices, e.g. a cellphone. Secondly, it does not require users to stay within the device's line-of sight, which is necessary for Kinect. Finally, unlike imaging tracking systems, it only detects location without other information or images of privacy. These three advantages ensure that this indoor FMCW radio tracking system has good potentials and is worthy of being studied in detail.

In addition to introduce the operational principles of the FMCW radio tracking system in two and three dimensions, this thesis has presented and made two important original contributions. First, a simulation model of the indoor FMCW radio tracking system is set up for the first time with MATLAB, with practical parameters, implementations and complete working process. It includes a FMCW signal generator, transmitting and rceving antennas, different channels and signal processing algorithms. With the model, the conventional FMCW tracking system is simulated under different channel conditions and its performances are evaluated for the first time.

The second contribution of this thesis is to propose two non-coherent detection methods by introducing Kurtosis CFAR and Skewness CFAR techniques to the FMCW tracking systems based on the statistic characteristic of the input signals. Not only have the principle and implementation been detailed, but also the influences of different parameters on the performance of the detection have been studied and the parameters for obtaining good performances are suggested.

The third contribution is to simulate the FMCW indoor tracking system of the conventional, Kurtosis and Skewness detections under AWGN, CM3 (LOS) and CM4 (NLOS) channels, respectively, using the simulation model developed in this thesis. The results shows that both of the two statistic-based detections (i.e., Kurtosis and Skewness) outperform the conventional CFAR detection to a great extent in all three channels (AWGN, CM3 and CM4), and the Skewness detection has a slightly better performance than the Kurtosis detection.

5.2 Future work

In this thesis, we first focus on the development of the simulation model of the Indoor FMCW radio tracking system. Then we work on the development of new novel detection methods based on Kurtosis and Skewness techniques.

However, in our work, we have not considered channel fluctuations and their impacts: performances of the tracking systems may be significantly different from the results we have obtained. This is a very interesting topic for future study. In addition, we have so far assumed one moving target. In practice, however, there may be more than one moving targets, e.g., multiple persons in a room. How to track multiple persons in an indoor environment is a topic of future study which is expected to be challenging.

Another issue that deserve to be investigated is the impact of narrow band interference (NBI). How Kurtosis detection and Skewness detection perform is very interesting and important to study, simply because narrow band interferences are common and do often exist in a real-world environment due to presence of many radio systems such as TV and civilian radio broadcasts.

REFERENCES

[1] Misra, P., & Enge, P. (1999). Special issue on global positioning system. *Proceedings of the IEEE*, *87*(1), 3-15.

[2] Want, R., Hopper, A., Falcao, V., & Gibbons, J. (1992). The active badge location system. *ACM Transactions on Information Systems (TOIS)*, *10*(1), 91-102.

[3] Want, R., & Hopper, A. (1992). Active badges and personal interactive computing objects. *IEEE Transactions on Consumer Electronics*, *38*(1), 10-20.

[4] Azuma, R. (1993). Tracking requirements for augmented reality. *Communications of the ACM*, *36*(7), 50-51.

[5] Varshavsky, A., De Lara, E., Hightower, J., LaMarca, A., & Otsason, V. (2007). GSM indoor localization. *Pervasive and Mobile Computing*, *3*(6), 698-720.

[6] Youssef, M., & Agrawala, A. (2005, June). The Horus WLAN location determination system. In *Proceedings of the 3rd ACM International Conference on Mobile Systems, Applications, and Services* (pp. 205-218).

[7] Bahl, P., Padmanabhan, V. N., & Balachandran, A. (2000). Enhancements to the RADAR user location and tracking system. *Microsoft Research*, *2*(MSR-TR-2000-12), 775-784.

[8] Bahl, P., & Padmanabhan, V. N. (2000). RADAR: An in-building RF-based user location and tracking system. In *Proceeding of the 9th Annual Joint Conference of the IEEE Computer and Communications Societies. Proceedings.* Vol. 2, 2000, pp. 775-784.

[9] Gwon, Y., & Jain, R. (2004, October). Error characteristics and calibration-free techniques for wireless LAN-based location estimation. In *Proceedings of the Second ACM International Workshop on Mobility Management & Wireless Access Protocols*, pp. 2-9.

[10] Lim, H., Kung, L. C., Hou, J. C., & Luo, H. (2005). Zero-configuration, robust indoor localization: Theory and experimentation. In *Infocom*, 2006

[11] Bahl, Ward, A., Jones, A., Hopper, A. (1997). A new location technique for the active office. In *IEEE Pers. Commun.*, vol.4, no.5, pp.42-47.

[12] Zhang, Z. (2012). Microsoft kinect sensor and its effect. *IEEE Multimedia*, 19(2), 4-10.

[13] Adib, F., Kabelac, Z., Katabi, D., & Miller, R. C. (2014, April). 3D tracking via body radio reflections. In *NSDI* (Vol. 14, pp. 317-329).

[14] Adib, F., Kabelac, Z., & Katabi, D. (2015, May). Multi-Person localization via RF body reflections. In *NSDI* (pp. 279-292).

[15] Adib, F., & Katabi, D. (2013). See through walls with WiFi! In *ACM SIGCOMM* (Vol. 43, No. 4, pp. 75-86).

[16] Lee, W. C., Hung, F. H., Tsang, K. F., Wu, C. K., & Chi, H. R. (2016, July). RSS-based localization algorithm for indoor patient tracking. In *Industrial Informatics (INDIN), 2016 IEEE 14th International Conference* (pp. 1060-1064).

[17] Winder, A. A. (1975). II. Sonar system technology. *IEEE Transactions on Sonics and Ultrasonics*, *22*(5), 291-332.

[18] Odendaal, J. W., Barnard, E., & Pistorius, C. W. I. (1994). Two-dimensional superresolution radar imaging using the MUSIC algorithm. *IEEE Transactions on Antennas and Propagation*, *42*(10), 1386-1391.

[19] Wu, Y., & Linnartz, J. P. M. G. (2011, May). Detection performance improvement of FMCW Radar using frequency shift. *In Proceedings of the 32nd WIC Symposium on Information Theory in the Benelux, Brussels, Belgium* (pp. 1-8).

[20] Griffiths, H. D. (1990). New ideas in FM radar. *Electronics & Communication Engineering Journal*, 2(5), 185-194

[21] Klauder, J. R., Price, A. C., Darlington, S., & Albersheim, W. J. (1960). The theory and design of chirp radars. *Bell Labs Technical Journal*, 39(4), 745-808.

[22] Tiebout, M. (2004). A CMOS direct injection-locked oscillator topology as high-frequency low-power frequency divider. *IEEE Journal of Solid-State Circuits*, *39*(7), 1170-1174.

[23] *Understanding the FCC regulations for low-power, non-licensed transmitters.* Office of Engineering and Technology Federal Communications Commission. (1993).

[24] Mahafza, B. R. (2002). Radar systems analysis and design using MATLAB. USA Florida: CRC press, 2000: 106-108 .

[25] Antoniou, A. (2016). *Digital signal processing*. McGraw-Hill.

[26] Stove, A. G. (1992, October). Linear FMCW radar techniques. In *IEEE Proceedings of Radar and Signal Processing*. Vol. 139, No. 5, pp. 343-350.

[27] Skolnik, M. (2001). Introduction to radar systems. *IEEE Aerospace and Electronic Systems Magazine*, 16(10), 19-19.

[28] Stutzman, W. L., & Thiele, G. A. (2012). *Antenna theory and design*. John Wiley & Sons.

[29] Rappaport, T. S. (1996). *Wireless communications: principles and practice* (Vol. 2). New Jersey: prentice hall PTR.

[30] Molisch, A. F., Balakrishnan, K., Chong, C. C., Emami, S., Fort, A., Karedal, J., ... & Siwiak, K. (2004). IEEE 802.15. 4a channel model-final report. *IEEE P802*, *15*(04), 0662.

[31] Braun, S. (1975). The extraction of periodic waveforms by time domain averaging. *Acta Acustica united with Acustica*, *32*(2), 69-77.

[32] Ristic, B., Arulampalam, S., & Gordon, N. J. (2004). *Beyond the Kalman filter: Particle filters for tracking applications*. Artech house.

[33] Meserve, B. E. (2014). *Fundamental concepts of geometry*. Courier Corporation.

[34] Macmillan, N. A. (2002). Signal detection theory. *Stevens' handbook of experimental psychology.*

[35] Wickens, T. D. (2002). *Elementary signal detection theory*. Oxford University Press, USA.

[36] Geisser, S., & Eddy, W. F. (1979). A predictive approach to model selection. *Journal of the American Statistical Association*, *74*(365), 153-160.

[37] Santoso, T. B., & Huda, M. (2015, September). Performance evaluation of CFAR detector for delay spread analysis of underwater acoustic channel. In *Electronics Symposium (IES), 2015 International* (pp. 173-177).

[38] Hyvärinen, A., Karhunen, J., & Oja, E. (2004). *Independent component analysis* (Vol. 46). John Wiley & Sons.

[39] Khan, M. G., Sallberg, B., Nordberg, J., & Claesson, I. (2009, September). Non-coherent detection of impulse radio UWB signals based on fourth order statistics. In *IEEE International Conference on Ultra-Wideband, ICUWB 2009.* (pp. 824-828).

[40] Corliss, G. (1977). Which root does the bisection algorithm find?. *Siam Review*, *19*(2), 325-327.

[41] Burden, R. L., & Faires, J. D. (1985). 2.1 The bisection algorithm. *Numerical Analysis. Prindle, Weber & Schmidt, Boston, MA., pp. x*, *676*.

[42] Ashkar, F., & Mahdi, S. (2006). Fitting the log-logistic distribution by generalized moments. *Journal of Hydrology*, *328*(3), 694-703.

[43] Kim, T. H., & White, H. (2004). On more robust estimation of skewness and kurtosis. *Finance Research Letters*, *1*(1), 56-73.

[44] Doane, D. P., & Seward, L. E. (2011). Measuring skewness: a forgotten statistic. *Journal of Statistics Education*, *19*(2), 1-18.

[45] Mardia, K. V. (1970). Measures of multivariate skewness and kurtosis with applications. *Biometrika*, *57*(3), 519-530.

[46] Moschopoulos, P. G. (1985). The distribution of the sum of independent gamma random variables. *Annals of the Institute of Statistical Mathematics*, *37*(1), 541-544.

[47] Gandhi, P. P., & Kassam, S. A. (1988). Analysis of CFAR processors in homogeneous background. *IEEE Transactions on Aerospace and Electronic systems*, 24(4), 427-445.

[48] Tabet, L., & Soltani, F. (2009). A generalized switching CFAR processor based on test cell statistics. *Signal, image and video processing*, *3*(3), 265-273.

[49] Cao, T. T. (2008). Constant false-alarm rate algorithm based on test cell information. *IET Radar, Sonar & Navigation*, *2*(3), 200-213.

[50] Erfanian, S., & Vakili, V. T. (2009). Introducing excision switching-CFAR in K distributed sea clutter. *Signal Processing*, *89*(6), 1023-1031.

[51] Magaz, B., & Belouchrani, A. (2011). Automatic threshold selection in OS-CFAR radar detection using information theoretic criteria. *Progress In Electromagnetics Research B*, *30*, 157-175.

[52] Liu, N. N., Li, J., & Cui, Y. (2010). A new detection algorithm based on CFAR for radar image with homogeneous background. *Progress In Electromagnetics Research C*, *15*, 13-22.

[53] Cook, D. J., Youngblood, M., Heierman, E. O., Gopalratnam, K., Rao, S., Litvin, A., & Khawaja, F. (2003, March). MavHome: An agent-based smart home. In *Proceedings of the First IEEE International Conference on Pervasive Computing and Communications, 2003,* pp. 521-524.